

# Mechanisms of Scaffold-Mediated Microcompartment Assembly and Size Control

Farzaneh Mohajerani, Evan Sayer, Christopher Neil, Koe Inlow, and Michael F. Hagan\*



Cite This: *ACS Nano* 2021, 15, 4197–4212



Read Online

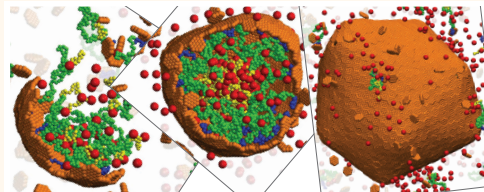
ACCESS |

Metrics & More

Article Recommendations

Supporting Information

**ABSTRACT:** This article describes a theoretical and computational study of the dynamical assembly of a protein shell around a complex consisting of many cargo molecules and long, flexible scaffold molecules. Our study is motivated by bacterial microcompartments, which are proteinaceous organelles that assemble around a condensed droplet of enzymes and reactants. As in many examples of cytoplasmic liquid–liquid phase separation, condensation of the microcompartment interior cargo is driven by flexible scaffold proteins that have weak multivalent interactions with the cargo. Our results predict that the shell size, amount of encapsulated cargo, and assembly pathways depend sensitively on properties of the scaffold, including its length and valency of scaffold–cargo interactions. Moreover, the ability of self-assembling protein shells to change their size to accommodate scaffold molecules of different lengths depends crucially on whether the spontaneous curvature radius of the protein shell is smaller or larger than a characteristic elastic length scale of the shell. Beyond natural microcompartments, these results have important implications for synthetic biology efforts to target alternative molecules for encapsulation by microcompartments or viral shells. More broadly, the results elucidate how cells exploit coupling between self-assembly and liquid–liquid phase separation to organize their interiors.



**KEYWORDS:** bacterial microcompartments, self-assembly, carboxysomes, protein shells, cargo encapsulation, liquid–liquid phase separation, simulation

While the eukaryotic cytoplasm is organized by lipid-encased organelles, it is now clear that cells from all kingdoms of life employ other modes of compartmentalization, such as liquid–liquid phase separation (LLPS)<sup>1–4</sup> and proteinaceous organelles.<sup>5–7</sup> For example, bacterial microcompartments are organelles that form by assembling a protein shell around a dense complex of enzymes and reactants in certain metabolic pathways.<sup>8–15</sup> The best-studied type of microcompartment is the carboxysome, which assembles around a dense complex of the enzyme ribulose-1,5-bisphosphate carboxylase/oxygenase (rubisco) and other proteins to facilitate the Calvin–Bensen–Bassham cycle in autotrophic bacteria.<sup>8,9,16,17</sup>

Other protein-shelled compartments are found in bacteria and archaea (e.g., encapsulins<sup>18,19</sup> and gas vesicles<sup>18,20</sup>) and eukaryotes (e.g., vault particles<sup>21</sup>). Microcompartment function depends crucially on the amount and composition of encapsulated cargo and the integrity of the surrounding shell. Thus, understanding the mechanisms that control cargo encapsulation and shell assembly is important to elucidate the normal biological functions of microcompartments and to re-engineer microcompartments as customizable nanoreactors for synthetic biology applications.<sup>12,22–35</sup>

More broadly, there are strong parallels between the condensed cargo within a microcompartment and liquid–liquid phase-separated fluid domains. For example, the rubisco complex within carboxysomes has a similar structure and function to the pyrenoid, which is a liquid-phase separated domain consisting of rubisco and other components that is found within plant cells.<sup>36–39</sup> Moreover, experiments and models suggest that microcompartment assembly proceeds by phase separation of the cargo, either prior to or during assembly of the outer shell.<sup>40–48</sup> However, the protein shell of a microcompartment confers distinct advantages over uncoated liquid domains. In addition to functioning as a selectively permeable barrier,<sup>49–51</sup> experiments suggest that the shell plays a structural role, influencing the size and morphology during microcompartment assembly.<sup>23,26,40,52–54</sup> Despite intense

Received: July 9, 2020

Accepted: March 3, 2021

Published: March 8, 2021



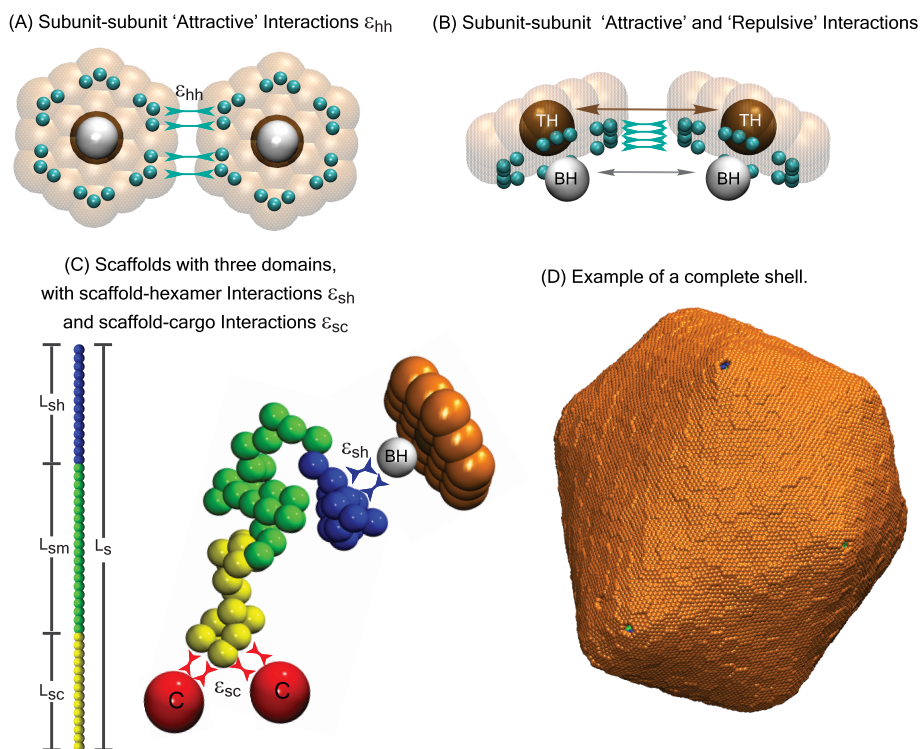


**Figure 1. Description of the computational model.** (A) Bottom and (B) side views of shell subunits. Each subunit contains “attractors” (cyan spheres) on its perimeter and a “top” (ochre sphere, “TH”) and a “bottom” (white sphere, “BH”) in the center above and below the subunit plane. Interactions between attractors drive subunit assembly, while top–top and bottom–bottom repulsions control the subunit–subunit angle and spontaneous curvature radius of the shell,  $R_0$ . (C) Scaffolds are bead–spring polymers with three domains: scaffold–cargo binding domain (yellow) beads have attractive interactions with cargo particles, middle domain (green) beads have no attractive interactions with cargo or shell subunits, and scaffold–subunit binding domain (dark blue) beads have attractive interactions with subunit bottom pseudoatoms “BH”. The contour length of the scaffold with  $N_s$  beads is denoted as  $L_s$ , while the lengths of the domains are  $L_{sc}$ ,  $L_{sm}$ , and  $L_{sh}$ , respectively. Excluder atoms (orange pseudoatoms in the plane of the “top”) experience excluded volume interactions with the cargo and scaffold beads. (D) Example of a complete shell with spontaneous curvature radius  $R_0 = 22$ , with encapsulated cargo and scaffold molecules with  $L_s = 64$  ( $L_{sc} = 7$ ,  $L_{sm} = 50$ ,  $L_{sh} = 7$ ). All lengths in this article are given in units of  $r^*$ , the cargo diameter (the rubisco diameter) in the carboxysome is  $\sim 13$  nm, and energies are in units of the thermal energy  $k_B T$ .

recent investigations into LLPS, we have yet to understand the role of LLPS in promoting or guiding self-assembly and cargo encapsulation or, conversely, the role of assembly in promoting and regulating LLPS. Thus, models that describe coupled LLPS and microcompartment assembly are needed to identify the factors that control microcompartment formation, cargo encapsulation, and function. From a practical perspective, condensation of cargo into fluid domains is a powerful approach to develop self-assembling and self-packaging gene/drug delivery vehicles.<sup>55–65</sup> Coupling such complexes to shell assembly could enable control of their size, amount of packaged cargo, and targeting capabilities.

Microcompartment shells are polydisperse (40–400 nm diameter), roughly icosahedral, and formed from pentameric, hexameric, and pseudo-hexameric (trimer-of-dimer) protein oligomers.<sup>8,9,17,53,66–70</sup> Recently, Sutter *et al.* obtained atomic-resolution structures of small (40 nm diameter) empty microcompartment shells composed of pentamer, hexamer, and pseudo-hexamer proteins<sup>53</sup> or smaller shells ( $\sim 20$  nm) composed of only pentamer and hexamer proteins.<sup>70</sup> While these structures provide essential insight into microcompartment architectures, the effect of cargo on shell assembly and the mechanisms that control cargo packaging remain unclear. In many types of microcompartments, cargo coalescence and cargo–shell interactions are mediated by auxiliary microcompartment proteins called scaffold proteins. Scaffold

proteins are typically flexible (e.g., the  $\alpha$ -carboxysome scaffold (CsoS2) is an intrinsically disordered protein) and contain multiple interaction sites with cargo molecules.<sup>37,43,45</sup> Thus, scaffolds drive cargo coalescence *via* weak multivalent interactions, paralleling mechanisms that drive liquid–liquid phase separation in cells.

Previous modeling studies have elucidated the assembly of empty icosahedral shells,<sup>71–97</sup> the effect of an interior template such as a nanoparticle or RNA molecule on shell assembly,<sup>78,84–86,98–122</sup> and how the interplay between template curvature and shell elasticity can control its size.<sup>78,106,107</sup> However, the many-molecule scaffold–cargo complex within a microcompartment does not have a specific size or morphology and, thus, requires alternative models. Recent computational works investigated assembly of microcompartment shell subunits<sup>123,124</sup> or assembly of shells around a single cargo species with direct pairwise attractions driving cargo coalescence and packaging.<sup>46–48</sup> These studies showed that the cargo can influence the size of the assembled shell through a kinetic mechanism<sup>48</sup> or a combination of kinetic and thermodynamic effects.<sup>46,47</sup> However, there are no models for microcompartment assembly that account for the crucial role of scaffold molecules.

Therefore, in this work we develop a computational model for microcompartment assembly that explicitly accounts for flexible scaffold molecules and scaffold-mediated cargo

coalescence and packaging. We are motivated by recent experiments that investigated how changing the length of the scaffold molecule affects the size of  $\alpha$ -carboxysome shells,<sup>45,125</sup> but the model is sufficiently general to also provide insights into self-assembling delivery vehicles.<sup>55–64</sup> In addition, we develop an equilibrium theory, which extends models for spherical micelles assembled from star or diblock copolymers,<sup>126–130</sup> to describe variable packaging of the interior block, and an exterior shell with a preferred curvature radius (which may differ from the preferred size of the micelle).

Our models predict that shell sizes increase with scaffold length over a broad range, but there are minimal and maximal sizes beyond which the shell size becomes independent of scaffold length. Cargo packaging diminishes with increasing scaffold length for fixed scaffold–cargo valence (*i.e.*, number of cargo interaction domains per scaffold molecule), eventually leading to sparsely filled shells. However, increasing the scaffold–cargo valence can restore full shells.

A scaling analysis suggests that microcompartment properties are determined by the relative values of characteristic length scales set by (i) the scaffold length, (ii) the spontaneous curvature of the protein shell, (iii) shell elasticity, and (iv) excluded volume. Our results show how these characteristic scales can be inferred from experimental measurements of the variation of shell size with scaffold length. Importantly, such measurements could reveal the role of shell spontaneous curvature in driving microcompartment closure, which is currently a key unresolved question.

## RESULTS AND DISCUSSION

**Computational Results.** To simulate scaffold-mediated microcompartment assembly, we extend a model with direct cargo–cargo and cargo–shell pair interactions<sup>47</sup> to include scaffold proteins (Computational Model section). Although we keep the model minimal to understand general principles, we are motivated by recent experiments on  $\alpha$ -carboxysome assembly.<sup>45,125</sup> The  $\alpha$ -carboxysome scaffold, CsoS2, contains three linearly connected flexible domains which include binding sites for the cargo (rubisco) and the shell proteins. Although the N-terminal domain contains multiple binding sites for rubisco, it is not known which sites interact with shell proteins. In many other microcompartment types, the scaffold molecules contain “encapsulation peptides” at their C-terminal domains that interact with the shell, but these have not been identified for CsoS2. Given the current level of experimental uncertainty, we have started with a simple model for the scaffold: a flexible bead–spring polymer with three domains (Computational Model section and Figure 1). The domain at one end has multiple cargo interaction sites, the domain at the other end binds to shell subunits, and the middle domain has only repulsive interactions with cargo and shell proteins. In future work we will explore other arrangements of interaction sites on the scaffold. To minimize the number of parameters, we restrict the computational model to a single size of cargo particles and scaffold segments. Thus, the simulations do not account for the small excluded volume size of a CsoS2 segment relative to a rubisco holoenzyme. However, we analyze effects of varying excluded volume using the theoretical model described below. To further focus on scaffold mediation, we restrict consideration to purely repulsive direct cargo–cargo and cargo–shell interactions, although attractive cargo–cargo and cargo–shell interactions have not been ruled out in the experimental systems.<sup>45,131</sup>

Natural microcompartment shells assemble from three classes of shell subunits (protein oligomers), each composed of proteins with different sequences: pentamers, hexamers, and “pseudo-hexamers” (trimers of heterodimers). Based on atomic-resolution structures of small empty microcompartment shells,<sup>70</sup> each subunit species has different preferred subunit–subunit angles, but hexamers are the major species by mass in large shells. Our goal in this work is to focus on the influence of scaffold molecules on microcompartment size. To this end, we employ a minimal model for shell assembly which includes only a single shell subunit species, which has hexamer symmetry but plays the role of *both* hexamers and pseudo-hexamers. Since AFM experiments have shown that microcompartment shell facets assemble from preformed oligomers,<sup>132</sup> we set the model hexamer as the basic assembly subunit (irreducible species) in our simulations.

Model subunits have attractive edge–edge interactions with a preferred angle that sets the intrinsic spontaneous curvature radius  $R_0$  of the shell. The spontaneous curvature of microcompartment shell proteins is not known. Hexamers may have zero spontaneous curvature, since systems of only hexamer proteins can form tubular structures or rolled sheets (rosettes) under some conditions,<sup>124,133–140</sup> and assemble flat sheets on surfaces or interfaces.<sup>132,141</sup> However, in the latter systems interfacial tension exerts a strong driving force favoring flat sheets. Moreover, recombinant expression of hexamers, pseudo-hexamers, and pentamers can result in small, icosahedral, empty shells,<sup>53,70,142</sup> implying that there is a net spontaneous curvature for at least some stoichiometries of microcompartment proteins. Given this uncertainty about spontaneous curvature, and since the subunits in our model account for both hexamers and pseudo-hexamers, we treat the spontaneous curvature radius  $R_0$  as a phenomenological parameter. We have also investigated the effect of  $R_0$  on microcompartment size in the case of assembly without scaffold proteins,<sup>47</sup> allowing us to focus on the effects of scaffold properties here. Additional model details are in the Methods section.

To elucidate assembly pathways and outcomes, we performed dynamical simulations over a range of scaffold lengths  $L_s$ , cargo-binding domain lengths  $L_{sc}$ , shell spontaneous curvature radii  $R_0$ , and binding affinities between scaffold–cargo, scaffold–subunit, and subunit–subunit pairs ( $\epsilon_{sc}$ ,  $\epsilon_{sh}$ ,  $\epsilon_{hh}$ ). Since empty microcompartment shells are rare in most natural systems, we consider subunit–subunit interaction strengths weak enough ( $\epsilon_{hh} < 3.3$  at  $R_0 = 4.5$ ,  $\epsilon_{hh} < 2.9$  at  $R_0 = 8.0$ , and  $\epsilon_{hh} < 2.8$  at  $R_0 = 22$ ) so that the presence of scaffold and cargo is required for nucleation. Moreover, previous computational and experimental studies have shown that assembly of well-formed shells requires moderate interaction strengths, since interactions that are too strong in comparison to the thermal energy lead to kinetic traps consisting of partial or incorrectly formed shells.<sup>46,47,83,92,93,122,143–155</sup> For most results in this work we maintain affinities ( $\epsilon_{sh} = 2.5k_B T$ ,  $\epsilon_{sc} = 1.0k_B T$ ) and a scaffold–cargo valence (number of cargo-binding sites,  $L_{sc} = 7$ ) that are sufficiently moderate that our simulations avoid such kinetic traps. We present results for three values of the spontaneous curvature radius,  $R_0 = 4.5$ , 8, and 22.0, which are respectively below, equal to, and above the size that is commensurate with the “wild-type” scaffold length in our model,  $L_s = 24r^*$  (see Methods).

*Assembly Pathways Depend on Scaffold–Cargo Interactions.* We find that the strength of scaffold-mediated cargo–

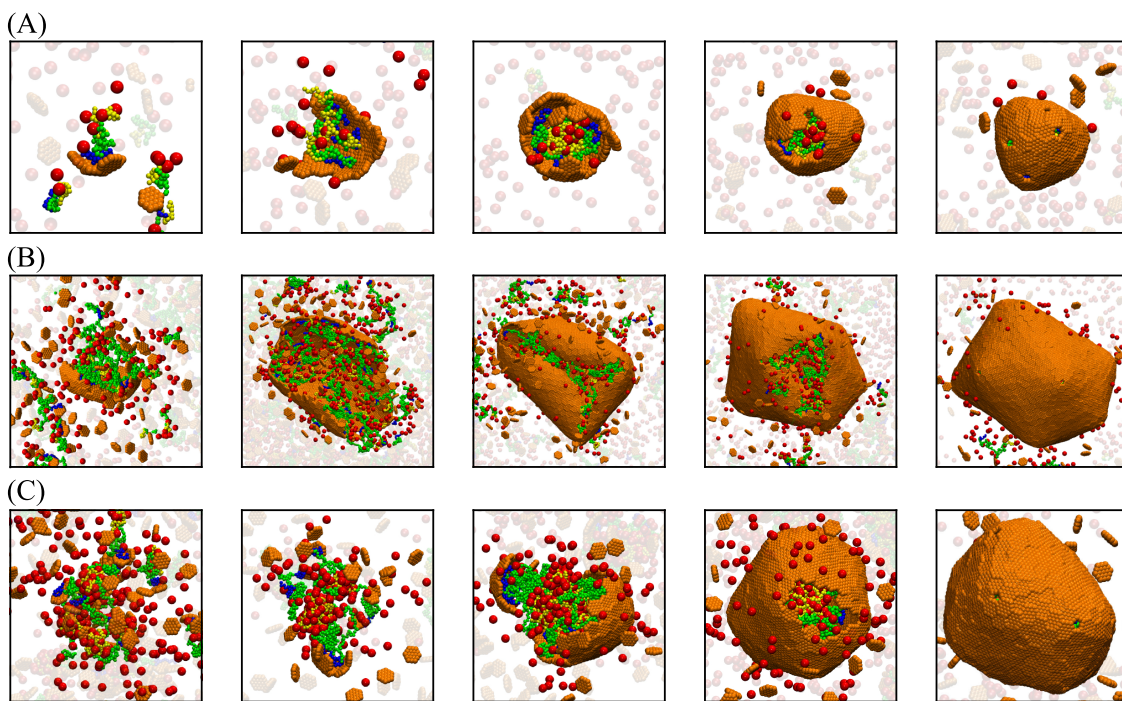


**Figure 2.** Snapshots from simulation trajectories illustrating typical assembly pathways and products (animations corresponding to these trajectories are provided in the *SI*, *videos*). (A) One-step assembly pathway leading to full shells: Coalescence of the cargo and scaffold occurs concomitantly with shell assembly. The mean size of assembled shells (defined as the radius of gyration of shell subunits) is  $R = 6.3 \pm 0.5$ . Parameter values are shell spontaneous curvature radius  $R_0 = 8.0$ , scaffold contour length  $L_s = 24$  ( $L_{sm} = 10$ ,  $L_{sc} = 7$ ), and subunit–subunit interaction strength,  $\epsilon_{hh} = 2.85$  (all lengths and energies are given in units of  $r^*$  and  $k_B T$ , respectively). (B) One-step assembly with sparse cargo loading, with mean shell size  $R = 18 \pm 3.6$ , for  $R_0 = 22$ ,  $L_s = 64$  ( $L_{sm} = 50$ ,  $L_{sc} = 7$ ), and  $\epsilon_{hh} = 2.65$ . (C) Two-step assembly pathway: The scaffold and cargo phase separate prior to shell assembly, due to increased valence of the scaffold–cargo binding domain,  $f_{sc} = 0.42$ . The shell size is  $R = 10.66 \pm 0.60$ . Parameter values are  $R_0 = 22$ ,  $L_s = 64$  ( $L_{sm} = 30$ ,  $L_{sc} = 27$ ), and  $\epsilon_{hh} = 2.65$ . For (A)–(C), the scaffold–shell and scaffold–cargo interaction strengths are  $\epsilon_{sh} = 2.5$  and  $\epsilon_{sc} = 1.0$ . Snapshots are shown at different scales for clarity.

cargo interactions strongly influences assembly pathways. Strong interactions ( $\epsilon_{sc} \gtrsim 1.2$  for the concentrations and wild-type cargo binding domain length used in our simulations) drive phase separation into a dilute phase and a high density liquid complex of scaffold and cargo molecules. This condition favors two-step assembly pathways (such as observed for assembly of  $\beta$ -carboxysomes<sup>40,41</sup>), in which the shell proteins adsorb onto the scaffold–cargo domain and then cooperatively into ordered shell structures. For weaker scaffold–cargo interactions, we observe one-step assembly pathways with simultaneous scaffold–cargo coalescence and shell assembly (Figure 2A,B). To quantitatively assess the extent to which a pathway is one-step or two-step, we have developed an order parameter that measures the number of adsorbed but unassembled subunits during a trajectory<sup>46</sup> (SI Figure S3D).

Here we are motivated by  $\alpha$ -carboxysomes, for which experiments observe one-step pathways and that the rubisco does not undergo phase separation in the absence of shell proteins at physiological conditions.<sup>43,69,156</sup> Therefore, for all further results we set  $\epsilon_{sc} = 1.0$ , which drives one-step assembly pathways for the wild-type scaffold and cargo-binding domain lengths.

In addition to classifying assembly pathways as one-step or two-step, we can further subdivide the one-step pathways into those that lead to full or empty shells. A set of snapshots from a typical assembly trajectory for each of these three categories is shown in Figure 2A,B,C, respectively, for (A) all scaffold domains at wild-type lengths and a commensurate shell

spontaneous curvature radius  $R_0 = 8$ , (B) a long middle domain and large preferred curvature  $R_0 = 22$ , and (C) a long cargo binding domain and  $R_0 = 22$ . Figure 2A and B correspond to clear one-step assembly pathways (as is the case for most parameters considered in this work). Assembly begins with a small aggregate involving all the microcompartment constituents: shell subunits, scaffold, and cargo. Because we focus on weak binding affinities, all these interactions are required to stabilize small aggregates. Consequently, the shell grows concomitantly with further coalescence of scaffold and cargo, until shell closure terminates assembly. While the scaffold and cargo are essential for nucleating assembly in both cases, the scaffolds with longer middle domains (which do not attract cargo particles in the model) lead to a lower density of packaged scaffold and cargo (Figure 2B) compared to the shorter middle domains (Figure 2A).

In contrast, the higher valence cargo-binding domain (Figure 2C) mediates cargo–cargo attractions that are nearly strong enough to drive phase separation, resulting in pathways closer to two-step assembly and full shells (SI Figure S3D). This result is consistent with experimental observations that  $\alpha$ -carboxysome scaffold and rubisco can phase separate without shell proteins under nonphysiological conditions.<sup>37,45</sup>

**Shell Size Depends on Scaffold Length.** We find that the shell size depends sensitively on scaffold length and shell spontaneous curvature. Motivated by the experiments, we vary the scaffold length above and below its wild-type length, with  $L_s = 24$  and  $L_{sc} = 7$  model segments roughly corresponding to the wild-type values for the total scaffold length and cargo

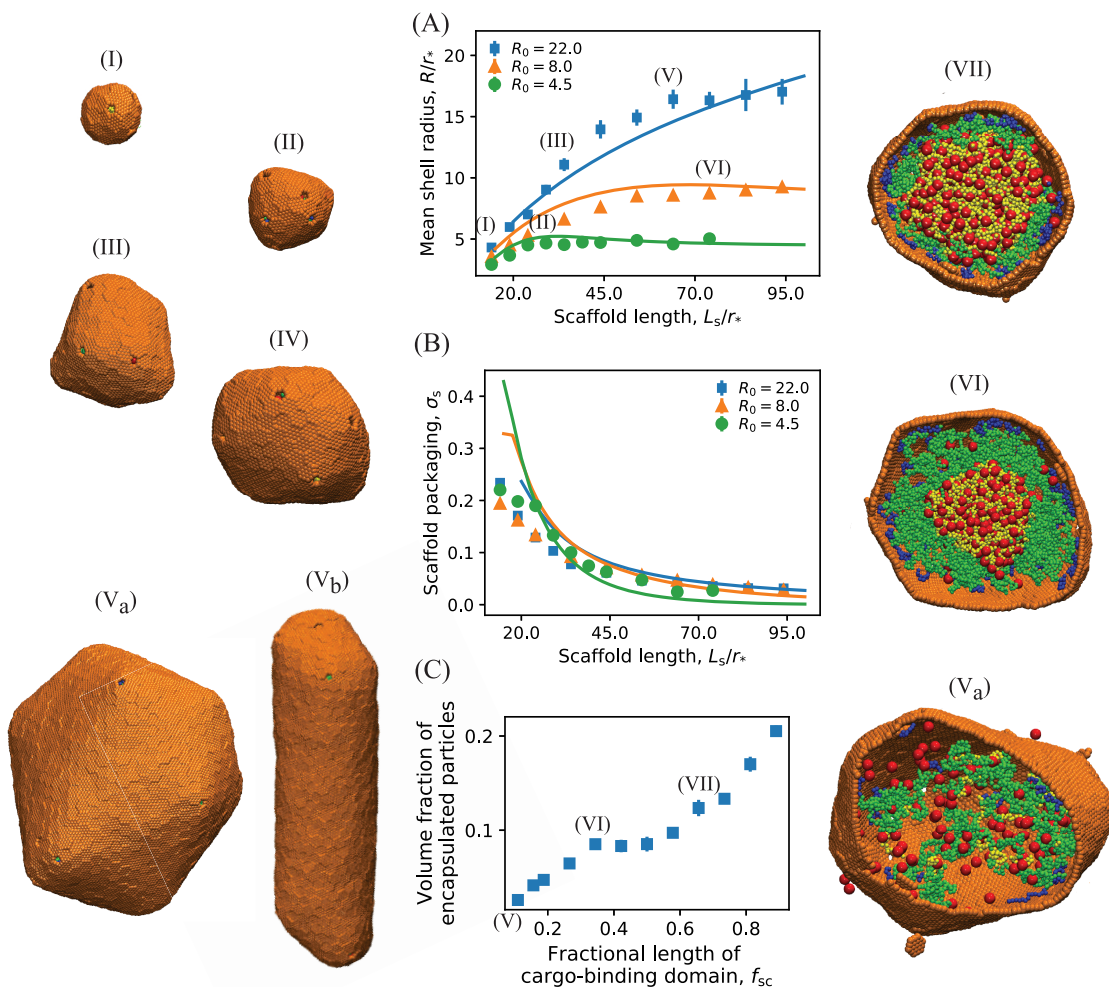


**Figure 3.** (A) Mean shell radius as a function of the scaffold length calculated from Brownian dynamics simulations (symbols) and the equilibrium theory (eq 1, lines). Results are shown for different shell spontaneous curvature radii:  $R_0 = 4.5$  (green ●), 8.0 (yellow ▲), 22.0 (blue ■). Example snapshots of assembled shells are shown to the left, taken from simulations with (I)  $R_0 = 22$ ,  $L_s = 14$ , (II)  $R_0 = 8$ ,  $L_s = 24$ , (III)  $R_0 = 22$ ,  $L_s = 34$ , (IV)  $R_0 = 8$ ,  $L_s = 74$ , and (V<sub>a,b</sub>)  $R_0 = 22$ ,  $L_s = 64$ . (B) Dependence of scaffold packaging on scaffold length and shell spontaneous curvature. The scaffold surface density (or ratio of packaged scaffold molecules to shell subunits,  $\sigma_s \equiv n_{scaf}/n_{shell}$ ) is shown for the same parameter values as in (A). In (A) and (B) the length of the middle domain of the scaffolds  $L_{sm}$  is varied, with fixed shell-interacting and cargo-interacting domain lengths  $L_{sh} = 7$  and  $L_{sc} = 7$ . The lines correspond to numerical minimization of eq 1, with respect to  $L_s \sim R_{scaf}^2$  and  $\sigma_s$ , with the scaffold chemical potential as an adjustable parameter set to  $\Delta\mu = -2.5k_B T$ . Other theory parameters are taken from the simulations: the scaffold bead excluded volume  $\nu = 0.065r_*^3$  and  $a\kappa = 12.5k_B T r_*^2$  (with  $a$  the subunit area and  $\kappa$  the bending modulus, which was approximately determined in ref 47). (C) Dependence of the volume fraction of encapsulated particles (cargo and scaffolds) on the fractional length of the cargo-binding domain of scaffolds  $f_{sc} = L_{sc}/L_s$ , for  $R_0 = 22$ ,  $L_s = 64$ , and  $L_{sh} = 7$ . Snapshots of the interior of shells assembled at different parameter values are shown on the right: (V<sub>a</sub>)  $f_{sc} = 0.11$ , (VI)  $f_{sc} = 0.27$ , (VII)  $f_{sc} = 0.58$ . Other parameter values for (A), (B), and (C) are as follows. Shell subunit–subunit affinities:  $\epsilon_{hh} = 3.15$  at  $R_0 = 4.5$ ,  $\epsilon_{hh} = 2.85$  at  $R_0 = 8.0$ , and  $\epsilon_{hh} = 2.65$  at  $R_0 = 22$ ; scaffold–shell interaction  $\epsilon_{sh} = 2.5$ , and scaffold–cargo interaction  $\epsilon_{sc} = 1.0$ .

binding domain length (see SI Section S2, Computational Model Details). Figure 3A shows the mean size of assembled shells as a function of the middle domain length  $L_{sm}$  (with the other two domains at constant lengths  $L_{sc} = 7$ ,  $L_{sh} = 7$ ) for several values of  $R_0$ . We identify two regimes, depending on whether the preferred size of the scaffold molecules (their end-to-end distance  $R_{scaf}$  in the absence of shell proteins, SI Figure S2) is smaller or larger than the intrinsically preferred shell size  $R_0$ . For small scaffold lengths,  $R_{scaf} < R_0$ , shell size increases with scaffold length, consistent with experimental observations,<sup>125</sup> until saturating at a value on the order of  $R_0$ . In this limit, the number of encapsulated scaffold molecules ( $n_{scaf}$ ) relative to shell subunits ( $n_{shell}$ ), given by  $\sigma_s = n_{scaf}/n_{shell}$ , decreases with increasing scaffold length (Figure 3B). Finally,

for  $R_{scaf} \gg R_0$  shells are unable to close around scaffold molecules, leading to incomplete assembly (SI Figure S7).

Although the total amount of packaged cargo increases with scaffold length for small lengths, due to the increasing shell size, the volume fraction of packaged cargo and scaffolds decreases monotonically with scaffold length (SI Figure S3A and B). That is, long scaffold middle domains lead to poor cargo loading, because the additional scaffold segments do not attract cargo but increase excluded volume in our computational model.

**Longer Cargo Binding Domains Increase Cargo Loading.** Figure 3C shows how cargo packaging depends on increasing the fractional length of the cargo binding domain,  $f_{sc} = L_{sc}/L_s$ , i.e., increasing  $L_{sc}$  at fixed  $L_s$ . We see that packaging increases

monotonically with  $f_{sc}$ , but there is an inflection point at  $f_{sc} = 0.3$  beyond which shells are nearly full. This point corresponds to the cargo binding domain length beyond which phase separation and two-step assembly pathways occur (SI Figure S3D). We find that two-step pathways always lead to full shells, but the shell size exhibits a very different dependence on parameters in comparison to the one-step cases we are focusing on. We plan to explore scaffold-mediated two-step assembly in detail in a future manuscript. This dependence on assembly pathways suggests that both thermodynamic and kinetic factors influence cargo packaging, as discussed further in the Conclusions section.

**Effect of Binding Affinity Values.** Finally, the shell size is relatively insensitive to the subunit–subunit  $\epsilon_{hh}$  and scaffold–subunit  $\epsilon_{sh}$  affinities, provided they are strong enough to drive assembly and scaffold packaging and weak enough to avoid kinetic traps and remain in the one-step regime (see SI Figure S3D). For example, decreasing  $\epsilon_{hh}$  leads to a small increase in shell size (20%) for spontaneous curvature radius  $R_0 = 8.0$  (SI Figure S6), whereas increasing the scaffold length effects a 3-fold increase in shell size for the same system (orange triangles in Figure 3A). However, higher values of the scaffold–cargo affinity  $\epsilon_{sc} \gtrsim 1.2$  lead to two-step assembly pathways.

**Shell Morphology.** In addition to size, scaffold properties influence shell morphologies. Simulations result in complete shells (other than the 12 5-fold vacancies required by topology) for most of the parameters we focus on here (SI Figure S7). However, the shells are not perfectly icosahedral, as shown by measurements of shell asphericity and the magnitude of icosahedral order in SI Figures S4 and S5, respectively. These results are consistent with the fact that natural microcompartments are predominately asymmetric;<sup>69,133</sup> in fact, Kennedy *et al.*<sup>133</sup> showed that protocols and techniques used to purify and image microcompartments with electron microscopy have overrepresented the degree of icosahedral symmetry.

As discussed below, these deviations from icosahedral symmetry likely reflect a combination of kinetic effects and energetic strain due to incompatibility between the preferred scaffold and shell sizes. In support of the latter effect, varying the scaffold far from the size that is commensurate with the preferred shell size leads to distinctive morphologies, in particular, elongated but complete shells (e.g., snapshot ( $V_b$ ) in Figure 3). Short scaffolds can also result in shells with octahedral symmetry or paired 5-fold vacancies (SI Figure S3), although these defects may be model-dependent because shells are strained far from their preferred size. Finally, as noted above, varying the scaffold even further from the preferred size leads to no assembly or incomplete shells.

**Equilibrium Theory. Model.** To further understand the interplay between scaffold and shell properties, we developed a simple equilibrium model (see SI Section S1, Equilibrium Theory). Although kinetic factors may be important as noted above, the thermodynamic model captures key trends observed in the dynamical simulations.

We make the following simplifying assumptions: extensions to eliminate these approximations are straightforward. First, we restrict the theory to spherical shells as observed for most parameter values in the simulations. Second, cargo molecules are implicitly represented by a net driving force for scaffold packaging  $\Delta\mu$  that accounts for scaffold–shell and scaffold–cargo attractive interactions, as well as the mixing entropy penalty for scaffold coalescence. We further assume that the

coalesced cargo and scaffold–cargo binding domains are concentrated in the shell interior, while the other end of the scaffold, the scaffold–shell binding domain, binds to the inner shell surface. Our model system can thus be thought of as a diblock copolymer spherical micelle,<sup>126–128,157–159</sup> except that the stoichiometry of the interior/exterior block is annealed, and there is an exterior shell with a preferred curvature that may be incommensurate with the optimal size of the micelle within. We discuss below the implications of model predictions for alternative scaffold packaging geometries.

The free energy (per shell subunit) of a shell with radius  $R$  and ratio of scaffold/shell subunits  $\sigma_s$  is given by

$$f_{\text{assem}} = f_{\text{shell}} + \sigma_s f_{\text{scaf}} + f_{\text{ent}} \quad (1)$$

$$f_{\text{shell}} = g_{\text{hh}} + \frac{a\kappa}{2} \left( \frac{2}{R} - \frac{2}{R_0} \right)^2 \quad (2)$$

$$f_{\text{scaf}} = k_B T \left( \frac{R}{R_{\text{scaf}}} \right)^2 + k_B T \left( \frac{R_{\text{scaf}}}{R} \right)^2 + \Delta\mu + \frac{3}{2} \frac{k_B T \nu \sigma_s N_s^2}{aR} \quad (3)$$

$$f_{\text{ent}} = k_B T \sigma_s \log \sigma_s + k_B T (1 - \sigma_s) \log (1 - \sigma_s) \quad (4)$$

Here  $f_{\text{shell}}$  gives the shell free energy, with the first term ( $g_{\text{hh}}$ ) the free energy per subunit due to subunit–subunit contacts (see SI Section S1, Equilibrium Theory, eq 8) and the second term describing the bending energy due to deviations from the shell spontaneous curvature, with  $a$  the subunit area and  $\kappa$  the bending modulus. For simplicity, we neglect contributions from the 12 5-fold defects that are required by topology in real and computational microcompartments. Including these will not qualitatively change the results (see SI Section S1, Equilibrium Theory, and ref 47). Then the first two terms in  $f_{\text{scaf}}$  give the entropic penalty for stretching or compressing scaffold molecules from  $R_{\text{scaf}}$ . The following two terms account for attractive scaffold–cargo and scaffold–shell interactions ( $\Delta\mu$ ) and excluded volume interactions, with  $\nu$  being the scaffold segment excluded volume. Finally,  $f_{\text{ent}}$  represents the mixing entropy of encapsulated scaffolds. The equilibrium shell size and scaffold loading are obtained by minimizing the total free energy of the system. In the thermodynamic limit, the distribution of shell sizes will be strongly peaked around the size that minimizes the free energy *per subunit* of the shell complex (see SI Section S1, Equilibrium Theory, and refs 47, 160).

**Comparison of Theory with Computational Results.** The solid lines in Figure 3A,B show the theory results, with the parameters  $a\kappa = 12.5k_B T r_*^2$  and  $\nu = 0.065r_*^3$  calculated from simulations and  $\Delta\mu$  as a fitting parameter chosen by eye. We set  $R_{\text{scaf}} = l_k N_s^{1/2}$  with  $l_k$  the statistical segment length, since the theory separately accounts for chain stretching and excluded volume (as in the Flory approximation<sup>161</sup>).

We find that the theory qualitatively captures the main features observed in the simulation results. In particular, the shell size increases with scaffold length, until saturating near  $R_0$  for long scaffolds, where excluded volume limits scaffold packaging. However, for simulations with  $R_0 = 22$ , longer scaffolds undergo limited coalescence in the center of the shell, causing the shell size to saturate at smaller scaffold lengths than predicted by the theory.

**Scaling Analysis and the Small Excluded Volume Limit.** Equation 1 predicts that the system behavior depends on

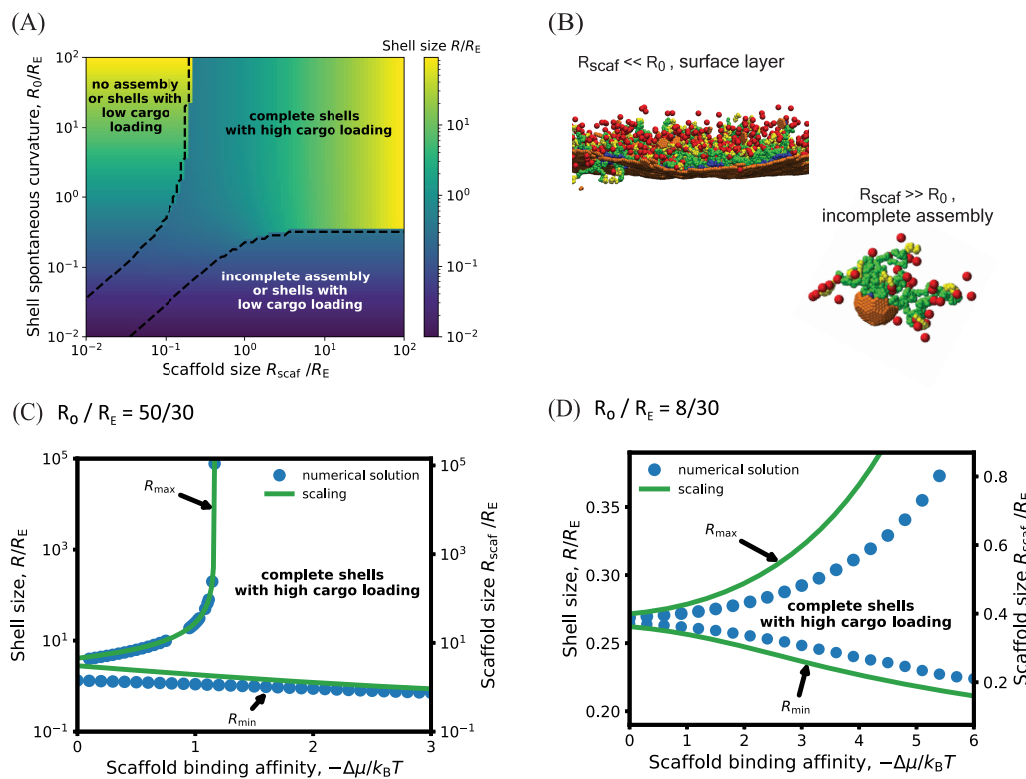


**Figure 4.** (A) Shell radius as a function of the shell spontaneous curvature radius  $R_0$  and scaffold unperturbed size  $R_{\text{scaf}}$  (normalized by the shell elastic energy length scale  $R_E$ ), calculated by numerically minimizing eq 1, with scaffold chemical potential  $\Delta\mu = -10k_B T$ ,  $R_E = 30$ , subunit area  $a = 2.5r_{*}^2$  and excluded volume parameter  $\nu = 0$ . The dashed line encompasses parameter values that lead to efficient scaffold packaging (see SI Figure S1 for the amount of packaged scaffold as a function of these parameters). Outside of this region  $\sigma_s \approx 0$ , leading to assembly of nearly empty shells (with a surface layer of scaffold and cargo) with sizes approximately equal to  $R_0$ , incomplete shells, or no assembly. The heat map in this region corresponds to the size of the complete but nearly empty shells. (B) Examples of incomplete assemblies that form in the dynamics simulations with overly short (top) or long (bottom) scaffold molecules. Parameters are (top)  $R_0 > 300$  and  $L_s = 34$ , (bottom)  $R_0 = 4.5$  and  $L_s = 84$ . Other parameters are as in Figure 3. (C) Minimum and maximum shell radii (normalized by the shell elastic energy length scale  $R_E$ ) that lead to assembly and cargo packaging, predicted by the theory for varying the scaffold length as a function of the scaffold packaging driving force  $\Delta\mu$ , for fixed shell spontaneous curvature  $R_0 = 50$ . The left y-axis shows the shell size, while the right y-axis shows the corresponding scaffold length, showing that the shell size closely tracks the scaffold preferred size in this regime. The symbols correspond to maximum and minimum shell sizes obtained by numerically minimizing eq 1, and the lines show the asymptotic results (eq 7). For scaffold lengths above the maximum length, shells would be either incomplete or empty, whereas below the minimum length, shells will either be incomplete or have low packaging of scaffold and cargo. (D) Minimum and maximum shell radius (normalized by  $R_E$ ) in the high intrinsic shell curvature regime ( $R_0 < R_E$ ), calculated by numerically minimizing eq 1 (symbols) and from the asymptotic analysis eq 11 (lines) for  $R_0 = 8$ ,  $R_E = 30$ , and  $\nu = 0$ . Other parameters in (C) and (D) are the same as in (A).

several characteristic length scales. In addition to the shell spontaneous curvature radius  $R_0$  and scaffold size  $R_{\text{scaf}}$ , we obtain length scales from the scaffold excluded volume,  $R_{\text{exc}} \sim (N_s \nu)^{1/3}$ , and the shell elastic energy,  $R_E = \sqrt{2ak/k_B T}$ . Specifically,  $R_E$  is the radius for which a closed shell with no spontaneous curvature  $R_0 = \infty$  would have a bending energy of  $k_B T$  per subunit. Different scaling forms can be deduced from eq 1 depending on the relative magnitudes of these lengths.

Since our model is most applicable to biological microcompartments in the limit of small excluded volume (see discussion), we focus here on the limit of small excluded volume,  $\nu \rightarrow 0$ . In SI section S1, Equilibrium Theory, we present a detailed derivation of these expressions and further analysis for finite excluded volume.

Figure 4 shows the shell size calculated as a function of scaffold length and shell spontaneous curvature with  $\nu = 0$ , by minimizing eq 1. The dashed black lines encompass the region with significant scaffold packaging for  $\Delta\mu = -10k_B T$ ; the full dependence of scaffold packaging on parameters is shown in SI Figure S1. We see that the range of accessible shell sizes

depends crucially on the relative sizes of the preferred shell curvature and the elastic length scale. For  $R_0 > R_E$  the shell size is highly tunable with scaffold length, varying over orders of magnitude, while only small deviations from the preferred shell curvature are possible in the opposite limit  $R_0 < R_E$ . This predicted trend may be a way to experimentally probe  $R_0$  in microcompartment systems.

**Scaling Analysis.** Further insight can be obtained from a simple scaling analysis. First, minimizing the free energy with respect to  $\sigma_s$  gives

$$\sigma_{\text{eq}} \approx 1/(1 + e^{f_{\text{scaf}}(R_{\text{eq}})/k_B T}) \quad (5)$$

Equation 5 shows that scaffold/cargo packaging diminishes as the shell size deviates from the preferred scaffold size  $R_{\text{scaf}}$ , but that scaffold can be packaged over a greater range of shell sizes by increasing  $|\Delta\mu|$ . Second, we obtain simplified expressions for the shell size and packaging depending on the relative characteristic scales as follows.

**Small Intrinsic Shell Curvature,  $R_0 \gg R_E$ .** In this limit the optimal shell size becomes asymptotically independent of shell

spontaneous curvature, and minimizing the free energy results in an optimal shell size:

$$R_{\text{eq}} \approx R_{\text{scaf}} \left[ 1 + \frac{1}{\sigma_{\text{eq}}} \left( \frac{R_E}{R_{\text{scaf}}} \right)^2 \right]^{1/4} \quad \text{for } R_0 \gg R_E \quad (6)$$

which can be further simplified in two limits:

$$R_{\text{eq}} \approx \begin{cases} R_{\text{scaf}} \left[ 1 + \frac{1}{\sigma_{\text{eq}}} \left( \frac{R_E}{2R_{\text{scaf}}} \right)^2 \right] \approx R_{\text{scaf}} & \text{for } R_{\text{scaf}} \gg R_E \\ (R_{\text{scaf}} R_E)^{1/2} \sigma_{\text{eq}}^{-1/4} & \text{for } R_{\text{scaf}} \ll R_E \end{cases} \quad (7)$$

Thus, the shell size depends on a competition between the preferred scaffold size and the tendency of the shell proteins to disfavor curvature: the shell size tracks the scaffold size  $R_{\text{eq}} \approx R_{\text{scaf}}$  for long scaffolds, but adopts the geometric mean of the scaffold size and shell elastic length for short scaffolds. These scaling estimates are compared against the full free energy in Figure 5A.

However, eq 5 shows that scaffold packaging will exponentially diminish for large deviations from  $R_{\text{scaf}}$ . Therefore, we estimate upper and lower bounds on the scaffold

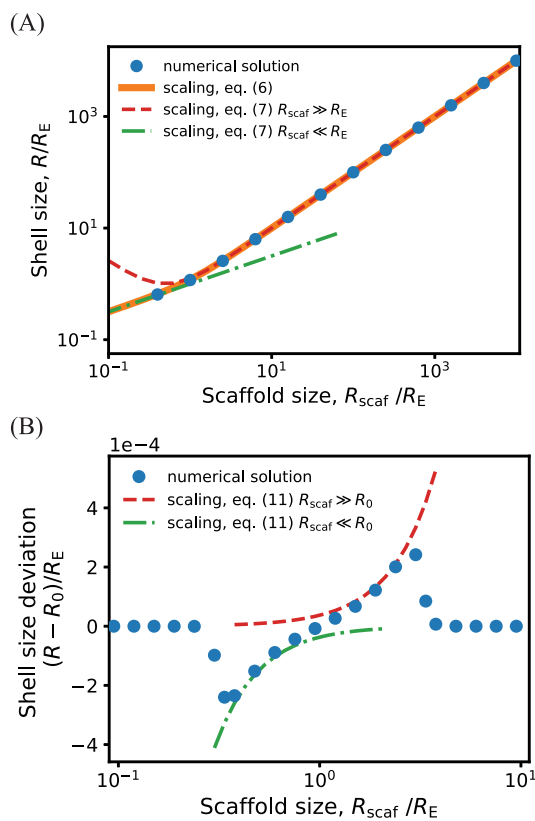


**Figure 5.** Dependence of shell size on the scaffold preferred size  $R_{\text{scaf}}$  calculated from the asymptotic analysis (lines, eqs 7 and 11), compared against numerical minimization of eq 1 (symbols). Results are shown in (A) and (B) respectively for shell spontaneous curvature radius values that are large or small compared to the shell elastic length scale: (A)  $R_0 = 300$  and (B)  $R_0 = 1$ , with  $R_E = 30$ . Other parameter values are  $a = 2.5r_*^2$ ,  $\Delta\mu = -10k_B T$ , and  $\nu = 0$ .

driven changes in shell size by noting that shell bending energy must be compensated by the free energy of scaffold packaging:

$$R_{\text{eq}}^{\text{max}} \approx \begin{cases} \frac{R_0 R_E}{R_E - (\Delta\mu_{\text{eff}}/k_B T)^{1/2} R_0}, & \text{for } (\Delta\mu_{\text{eff}}/k_B T)^{1/2} < \frac{R_E}{R_0} \\ \infty, & \text{for } (\Delta\mu_{\text{eff}}/k_B T)^{1/2} \geq \frac{R_E}{R_0} \end{cases} \quad (8)$$

$$R_{\text{eq}}^{\text{min}} \approx \frac{R_0 R_E}{R_E + (\Delta\mu_{\text{eff}}/k_B T)^{1/2} R_0} \approx R_E/(\Delta\mu_{\text{eff}}/k_B T)^{1/2}, \quad \text{for } R_0 \rightarrow \infty \quad (9)$$

with  $\Delta\mu_{\text{eff}} \equiv -(\Delta\mu + 2k_B T)\sigma_{\text{eq}} - f_{\text{ent}}$  the effective confinement free energy per shell subunit, since  $f_{\text{scaf}} \approx \Delta\mu + 2k_B T$  for  $R \approx R_{\text{scaf}}$  and

$$\sigma_{\text{eq}} \approx 1/(1 + e^{\Delta\mu/k_B T + 2}) \quad (10)$$

The packageable range of scaffold lengths can then be determined by combining eqs 8, 9, and 7 (Figure 4C). Outside of these bounds, scaffold packaging decreases exponentially, resulting in either no assembly or assembly of empty shells with sizes near  $R_0$ . Alternatively, for small scaffolds, if the scaffold–shell energy is sufficient to drive scaffold packaging without cargo, the scaffold can form a layer in the vicinity of the shell surface (Figure 4B). That scenario is not accounted for in the theoretical model.

Importantly, in any of these scenarios, the microcompartments will saturate at a *minimum* shell size with decreasing scaffold length (eq 9), which is an experimentally testable prediction.

**High Intrinsic Shell Curvature,  $R_0 < R_E$ .** In this regime the preferred curvature of the shell proteins influences the assembled shell size, so we must consider the full free energy, eq 1. Then, the limits in which the preferred scaffold size is larger or smaller than  $R_0$  result in

$$R_{\text{eq}} \approx \begin{cases} R_0 [1 + \sigma_{\text{eq}} (R_{\text{scaf}}/R_E)^2], & \text{for } R_{\text{scaf}} \gg R_0 \\ R_0 \left[ 1 - \frac{\sigma_{\text{eq}} R_0^4}{R_{\text{scaf}}^2 R_E^2} \right], & \text{for } R_{\text{scaf}} \ll R_0 \end{cases} \quad (11)$$

showing that the shell size depends on the competition between the shell spontaneous curvature and scaffold size, with their relative importance determined by the shell bending modulus (*via*  $R_E$ ). As above, there are bounds on the range of scaffold lengths that can be efficiently packaged, which increase with  $|\Delta\mu|$ . Since the shell bending energy dominates in this limit, the shell size exhibits only small deviations from  $R_0$  (Figure 5B), and the extent of scaffold incorporation is determined by the competition between the packaging driving force  $\Delta\mu$  and the scaffold confinement free energy  $f_{\text{scaf}}$  resulting in

$$R_{\text{scaf}}^{\text{min/max}} \approx R_0 \left[ \frac{1}{\Delta\mu_{\text{eff}}/k_B T - 1} \pm 2\sigma_{\text{eq}} \left( \frac{R_0}{R_E} \right)^2 \right]^{-1/2} \quad (12)$$

The range of shell sizes ( $R_{\text{eq}}^{\text{min}}$ ,  $R_{\text{eq}}^{\text{max}}$ ) can then be determined by combining eqs 10–12. Consistent with the numerical solution (Figure 4D), the range of accessible shell sizes is considerably smaller than in the large  $R_0$  limit (Figure 4C).

## CONCLUSIONS

We have theoretically and computationally investigated the equilibrium behavior and dynamical assembly pathways of a system in which polymeric scaffold molecules drive coalescence of many cargo particles and their packaging within an assembling protein shell. While motivated by bacterial microcompartments, we have employed minimal models allowing for generic conclusions about such multicomponent assemblies. Thus, in addition to elucidating the behaviors of natural and re-engineered bacterial microcompartments, our results suggest design principles for tailoring the size, morphology, and loading of synthetic or biomimetic systems such as delivery vehicles.

We find that the shell size and the amount of packaged cargo are determined by several characteristic length scales: the preferred sizes of the protein shell and the scaffold, the scaffold excluded volume size, and a characteristic elastic length scale of the shell (which depends on its rigidity). In our computational model, we have considered a relatively low bending rigidity of the shell (motivated by experimental observations on bacterial microcompartments), and scaffold excluded volume plays a significant role. In this case, results depend on whether the preferred scaffold size is either smaller than or larger than the spontaneous curvature radius. In the limit of small scaffold molecules, assembly driving forces are dominated by stretching of the scaffold between the cargo-filled interior and the surface of the protein shell, leading to shells that are smaller than the spontaneous curvature radius (provided that the scaffold–shell interactions and scaffold-mediated cargo–cargo interactions are stronger than shell bending elasticity). In the opposite limit of long scaffold molecules, scaffold packing becomes a dominant contribution, leading to decreased scaffold–cargo packaging and a shell size that roughly saturates at the spontaneous curvature radius and/or elongated shells.

Our simulations also demonstrate that the amount and morphology of packaged cargo depends on the strength and geometry of scaffold–cargo interactions. Multivalent scaffold–cargo interactions are essential for achieving full shells, while the scaffold length and distribution of cargo binding sites on the scaffold influence the morphology of the packaged cargo. When cargo-binding sites are limited to one end of long scaffold molecules, with scaffold–shell interactions at the other end, we observe a trilayer micelle-like complex, with an interior core of cargo, surrounded by a layer of scaffold, and finally the shell on the exterior. In contrast, longer scaffold–cargo binding domains or shorter scaffolds lead to a nearly uniform distribution of cargo and scaffold in the shell interior.

Because our primary objective was to qualitatively understand scaffold-mediated shell assembly, we did not tune the computational model parameters to match a specific biological system, and the computational model likely overestimates the scaffold excluded volume compared to bacterial microcompartments. For example, the  $\alpha$ -carboxysome scaffold (CsoS2) accounts for only 12% by mass of a wild-type  $\alpha$ -carboxysome,<sup>162</sup> compared to 70% in our model. Moreover, while we have included very weak scaffold inter-segment attractions in our model, stronger inter-segment attractions among CsoS2 residues could further reduce the effective excluded volume.

Therefore, we also developed a more tractable, though simplified, equilibrium theoretical model that facilitates more direct comparisons against experiments. Using this model, we

have explored a wide parameter range, including the effect of reducing the excluded volume. The theoretical analysis suggests that the ability of a scaffold to modulate shell size depends crucially on whether the protein shell spontaneous curvature radius is large or small compared to its elastic length scale. In the regime of a large spontaneous curvature radius, shell size is extremely malleable and can be tuned over a wide range by varying scaffold length. In contrast, shell proteins with a small preferred curvature radius exhibit only small size fluctuations and relatively poor packaging of scaffold molecules with incommensurate sizes. In both regimes, the range of scaffold lengths that can be packaged effectively and, correspondingly, the range of accessible shell radii increase with the free energy driving force for scaffold incorporation. This important control parameter depends on the scaffold concentration and the valence and affinity of the scaffold–cargo and scaffold–shell domains.

**Testing against Experiments.** Since our models are general, these predictions could be tested in a variety of biological or synthetic systems. For example, testing in bacterial microcompartments will be enabled by the modular nature of microcompartment scaffold molecules: the CsoS2 scaffold of the  $\alpha$ -carboxysome can be represented as a triblock copolymer, with the cargo-binding domain in the N-terminal block and shell-binding sites in the C-terminal block. Our results could thus be compared against experiments in which mutagenesis<sup>45</sup> is used to change the length of the middle domain (Figure 3A,B) or the cargo-binding domain (Figure 3C), although we note that the presence of shell binding sites in the middle block has not been ruled out.

Importantly, our results suggest a path to assess the magnitude and importance of the spontaneous curvature, a key unresolved question in microcompartment assembly. In particular, recent experiments on recombinant systems exhibit assembly of small ( $\sim$ 20–30 nm) empty microcompartment shells, suggesting a small shell spontaneous curvature radius. Yet, other experiments observe extensive flat sheets of hexamers,<sup>124,132–141</sup> suggesting the possibility of a low or zero spontaneous curvature. In this regard, both the simulations and theoretical model predict that shells with a small spontaneous curvature radius exhibit only narrow fluctuations in size when presented with scaffolds in molecules of different lengths, whereas shells with a large spontaneous curvature radius can assemble over a wide range of sizes to accommodate scaffolds with different lengths. In the small spontaneous curvature radius regime, our results suggest that preferred shell curvature plays a key role in driving shell closure, whereas in the large curvature radius regime scaffold properties (this work) and cargo properties<sup>47,48</sup> are important for shell closure.

One readily testable prediction from our model is that there is a minimum accessible shell size. Reducing scaffold lengths below this limit will lead to either a saturating shell size with diminished scaffolding packaging or abrogation of shell assembly.

**Kinetic and Thermodynamic Effects Drive Deviations from Icosahedral Symmetry.** Previous equilibrium elasticity studies of shells have identified local minima as a function of size at a series of “magic number” sizes, for which the structures have icosahedral symmetry or other high symmetries.<sup>71–73,89,106,107,121,122,163–165</sup> Yet, the assembly products in our simulations are predominately asymmetric, consistent with the structures of natural microcompartments.<sup>133</sup> This lack of

symmetry can be explained by three factors, the first kinetic and the other two thermodynamic. First, trajectories in our simulations and experimental systems begin from a highly out-of-equilibrium condition of dispersed subunits and, thus, are not guaranteed to approach equilibrium on the finite time scales of experiments and our simulations.<sup>154</sup> It is well known that overly strong interactions lead assembly into kinetic traps consisting of incomplete shells, due to free subunit starvation, or shells that cannot close due to defects.<sup>46,47,83,92,93,122,143–155,166</sup> In this work we focus on moderate binding affinities, and thus (except for very short or long scaffolds) most simulations lead to complete shells with the 12 S-fold defects required by topology. However, once a shell is complete, reorganization of its components is slow in comparison to assembly time scales, and thus diffusion of defects or changing the number of subunits to a size that is compatible with icosahedral symmetry does not occur on experimentally relevant time scales. Further, we find that switching from one-step to two-step assembly pathways is correlated to an increase in cargo loading (Figure 3C), suggesting that kinetic effects influence cargo encapsulation. However, the relatively strong agreement between our equilibrium theory and the dynamical simulation results (Figure 3A,B) suggests that the assembly products are *near* equilibrium for the moderate binding affinity parameter sets we have focused on.

In addition to kinetic effects, there are (at least) two sources of elastic strain that may suppress icosahedral symmetry. First, scaffolds with preferred sizes that are much smaller or larger than the shell spontaneous curvature radius lead to incomplete assembly. More moderate incompatibilities between preferred scaffold and shell size lead to complete but asymmetric shells, such as elongated shells (Figures 3 and S4). Second, formation of icosahedral structures from more than 60 asymmetric subunits requires multiple subunit species and/or elastic strains. Because our minimal model includes only a single subunit species, there are necessarily strains even in symmetric ground states. However, natural microcompartments also have far fewer shell protein species than the number of distinct local symmetry environments (the triangulation number  $T$ ).<sup>167</sup> Even a small shell with diameter  $d \approx 100$  nm has  $T = 75$ , and the triangulation number grows as  $T \propto d^2$ . Thus, natural microcompartment shells must have some degree of elastic strain.

**Coupling of Assembly to Liquid–Liquid Phase Separation.** While the discussion above focuses on the effect of a phase separating domain on the size and morphology of the assembling shell, our results demonstrate that the coupling between assembly and LLPS is bidirectional. Shell assembly can control both the onset of LLPS and the nature of its aggregation behavior. In particular, for low scaffold–cargo valences, shell assembly is required for nucleation and subsequent coalescence of the cargo domain. For larger scaffold–cargo valences, the cargo–scaffold complex domain nucleates spontaneously, but will undergo unbounded growth (until depleting cargo or scaffold) unless restrained by shell assembly. Thus, coupling to protein assembly can qualitatively change liquid domain formation from macrophase separation to self-limited assembly (aggregation). However, we reiterate that the preferred size of the domain is controlled by properties of both the shell and the encapsulated cargo.

**Outlook.** Finally, our results suggest additional physical ingredients that will be important to study for understanding

biological microcompartments or guiding the design of synthetic delivery vehicles. First, increasing the rigidity of the scaffold molecules would diminish the range of variation of shell sizes. This trend can be seen from the equilibrium scaling of the shell size in eqs 7 and 11, since the unperturbed scaffold size increases with its rigidity. Second, combining direct cargo–cargo interactions with scaffold mediation could enhance cargo packaging within assembling shells. This proposition is based on our observation in this work that increasing effective scaffold-mediated cargo interactions promotes cargo loading and is consistent with observations from previous models with cargo coalescence driven only by direct cargo–cargo pair interactions.<sup>46</sup> Third, although we observe qualitative agreement between our dynamical simulation results and the equilibrium theory, kinetic effects likely play important roles in some parameter regimes. For example, we have primarily focused on parameters that lead to one-step assembly pathways as observed for  $\alpha$ -carboxysomes, but we anticipate that kinetic effects will become more important in the case of two-step assembly pathways. Thus, models such as developed here, combined with experiments on different microcompartment systems and solution conditions, are needed to fully understand the interplay between thermodynamics and kinetics in scaffold-mediated shell assembly and cargo packaging.

## METHODS

**Computational Model.** Our computational model extends a previous model for assembly of a shell around fluid cargo<sup>46,47</sup> to include scaffold molecules and scaffold-mediated cargo–cargo and cargo–shell interactions. To focus on the effect of scaffold-mediated cargo interactions, we do not include direct cargo–cargo and cargo–shell attractive interactions, and we consider only one shell subunit species, which represents both hexamer and pseudo-hexamer proteins.

**Scaffolds.** In carboxysome systems, attractions between rubisco particles are mediated by auxiliary proteins (e.g., the intrinsically disordered protein CsoS2 in  $\alpha$ -carboxysomes<sup>43,45</sup> and the protein CcmM in  $\beta$ -carboxysomes<sup>40</sup>). The  $\alpha$ -carboxysome scaffold molecule, CsoS2, contains three linearly connected flexible domains, with the C-terminal domain containing multiple binding sites for the cargo molecule rubisco. While there is not yet clear experimental evidence for the location of the shell binding sequences, in  $\beta$ -carboxysomes and other microcompartments, shell–cargo attractions are mediated by an “encapsulation peptide” sequence in the N-terminal domain of the scaffold.<sup>23,31,40,168,169</sup> Motivated by these characteristics, we model the scaffold as a flexible bead–spring polymer with three linearly connected domains: a scaffold–cargo binding domain at one end with multiple cargo interaction sites, a scaffold–shell binding domain at the other end with multiple shell subunit binding sites, and a middle domain that has only repulsive interactions with cargo and shell proteins. Based on experimental evidence, we include weak attractive interactions between pairs of scaffold beads.

The interactions between various molecule types are modeled as follows, with further details given in SI Section S2, Computational Model Details.

**Scaffold–Cargo Interactions.** Attractive interactions between cargo particles and the “cargo-interacting” beads (type “SC”) in scaffolds are modeled by a Lennard-Jones potential with well-depth parameter  $\epsilon_{sc}$ .

**Scaffold–Shell Interactions.** Attractive interactions between subunits and scaffolds are modeled by a Morse potential with well-depth parameter  $\epsilon_{sh}$  between beads in “shell interacting” beads in polymers (blue beads in Figure 1C) and bottom pseudoatoms on subunits (type “BH”). We also add a layer of “excluders” in the plane of the “top” pseudoatoms, which account for shell–scaffold and shell–cargo excluded volume interactions.

**Table 1. Computational Model Parameters and Variables**

parameter/variable	symbol
shell radius	$R$
surface density of encapsulated scaffolds	$\sigma_s$
shell spontaneous curvature radius	$R_0$
total length of scaffold	$L_s$
length of scaffold shell binding domain	$L_{sc}$
length of scaffold cargo binding domain	$L_{sh}$
length of scaffold middle domain	$L_{sm}$
number of segments in scaffold	$N_s$
scaffold statistical segment length	$l_k$
excluded volume of a scaffold segment	$\nu$
subunit area	$a$
shell bending modulus	$\kappa$
number of subunits in a shell	$n_{shell}$
number of encapsulated scaffolds in a shell	$n_{scaf}$
subunit–subunit interaction	$\epsilon_{hh}$
scaffold–subunit interaction	$\epsilon_{sh}$
scaffold–cargo interaction	$\epsilon_{sc}$

**Subunit–Subunit Interactions.** Interactions between edges of BMC shell proteins are primarily driven by shape complementarity and hydrophobic interactions.<sup>53</sup> To mimic these short-ranged directionally specific interactions, each model subunit contains “attractors” on its perimeter that mediate subunit–subunit attractions. Complementary attractors on nearby subunits have short-range interactions (modeled by a Morse potential, eq S28 in SI Section S2, Computational Model Details). Attractors that are not complementary do not interact. The arrangement of attractors on subunit edges is shown in Figure 1, with pairs of complementary attractors indicated by cyan double-headed arrows. The subunit–subunit binding affinity is proportional to the well depth of the Morse potential between complementary attractors, given by  $\epsilon_{hh}$ .

To control the shell spontaneous curvature and bending modulus, each subunit contains a “top” (type “TH”) pseudoatom above the plane of attractors and a “bottom” pseudoatom (type “BH”) below the attractor plane. There are repulsive interactions (WCA interactions, eq 27) between top–top, bottom–bottom, and top–bottom pairs of pseudoatoms on nearby subunits. The relative sizes of the top and bottom pseudoatoms set the preferred subunit–subunit binding angle (and thus the spontaneous curvature  $R_0$ ), while the interaction strength (controlled by the well-depth parameter  $\epsilon_{angle}$ ) controls the shell bending modulus  $\kappa$ . The top–bottom interaction ensures that subunits do not bind in inverted orientations.<sup>79</sup> Since the subunit–subunit interaction geometries are already controlled by the attractor, top, and bottom pseudoatoms, we do not consider excluder–excluder interactions.

**Effects of Simplifying the Shell Stoichiometry.** To focus on the effects of scaffold properties on microcompartment assembly, we have employed a minimal shell protein model with only a single hexameric subunit species with spontaneous curvature, meant to represent both hexamers and pseudo-hexamers. We neglect pentamers based on our previous computational study<sup>47</sup> and experiments on assembly of  $\alpha$ -carboxysome systems in the absence of pentamer proteins.<sup>170,171</sup> In previous simulations, we found that the stoichiometric ratio of pentamers to hexamers affects the size of assembled shells, and one can expect that the stoichiometric ratio of pseudo-hexamers plays a role as well. However, based on their mass percentage in purified BMCs, pentamers are likely present in cells at very low stoichiometric ratios compared to other subunit species. We found that a system of only hexamer subunits can assemble shells with morphologies similar to those obtained at low stoichiometric ratios of pentamers, except that the shells in the hexamer-only system each contain 12 vacancies. Despite these vacancies, the entire scaffold remains inside complete shells due to scaffold–cargo and scaffold–subunit interactions on the two end domains of the scaffold molecules. Moreover, if pentamers

are introduced after assembly, they can fill in these vacancies, leading to complete shells.<sup>47</sup>

These computational results are consistent with experimental observations on assembly of  $\alpha$ -carboxysomes in the absence of pentamer proteins. Cai *et al.*<sup>170</sup> showed that deleting the pentamer proteins (CsoS4) in *H. neapolitanus* resulted in structures that were predominantly similar to those assembled with pentamers, although there were some elongated shells. Function was impaired, but could be restored by adding pentamers to the system after assembly. More recently, Long *et al.*<sup>171</sup> performed recombinant experiments in tobacco plants, showing that expressing only the scaffold (CsoS2) and hexamer protein (CsoS1A) from *Cyanobium marinum* PCC7001  $\alpha$ -carboxysomes is sufficient to obtain shells with normal appearance and at least partial function. However, while these results suggest that eliminating pentamers has only a minor effect on  $\alpha$ -carboxysome assembly, deleting pentamers (and in some cases pseudo-hexamers) in other types of microcompartments ( $\beta$ -carboxysomes and Pdu) led to more significant structural aberrations, including elongated shells.<sup>124,133–140,171–176</sup> Overexpressing hexamers also resulted in elongated structures,<sup>40</sup> although that may be caused in part by the increased hexamer/pseudo-hexamer stoichiometry. Intriguingly, experiments suggest that  $\alpha$ -carboxysomes assemble by one-step assembly pathways, whereas  $\beta$ -carboxysomes and Pdu microcompartments follow two-step pathways, suggesting that pentamers may have different effects depending on the assembly pathway.

Note that curvature in our model arises only due to angles between the rigid body subunits, whereas the experimental structure of Tanaka *et al.*<sup>177</sup> suggests the possibility of intrasubunit bending for pseudo-hexamers. While we plan to explore this possibility in a future work, this additional degree of freedom should not qualitatively change the dependence of shell size on scaffold properties, which is the focus of this work.

**Simulations.** We simulated assembly dynamics using the Langevin dynamics algorithm in HOOMD (which uses GPUs to efficiently simulate dynamics<sup>178</sup>) and periodic boundary conditions to represent a bulk system. The subunits were modeled as rigid bodies.<sup>179</sup> Each simulation was performed in the NVT ensemble, using a set of fundamental units<sup>180</sup> with the unit length scale  $r_*$  defined as the cargo particle diameter, and energies in units of the thermal energy,  $k_B T$ . The simulation time step was 0.005 in dimensionless time units, and we performed  $2 \times 10^8$  time steps in each simulation, except the maximum simulation time was increased to  $4 \times 10^8$  for  $L_s \geq 40$  and  $R_0 = 22$  (because longer time scales were required for the large shells that assemble at those parameters).

**Systems.** Each system included 2300 shell subunits, 2000 cargo particles, and 213 scaffold molecules in a cubic box with side length  $120r_*$ . To avoid overlaps in the initial condition, simulations were initialized by placing subunits and cargo particles on a grid, with scaffolds in extended configurations in between. Initial subunit orientations were random. For systems near the threshold for cargo–scaffold phase separation ( $L_{sc} > 7$ ), we eliminated correlations imposed by the grid by performing an initial dynamics with excluded volume interactions only (all attractive interactions turned off) for  $5 \times 10^6$  time steps. The attractive interactions were turned on after completion of this initialization dynamics. For other parameter sets, this initial dynamics protocol was not needed since memory of the initial condition was lost before any assembly began.

**Sample Sizes.** We performed a minimum of 10 independent trials at each parameter set and performed additional trials if needed so that at least 10 complete shells formed among all trials at a given parameter set. In particular, simulations with a large spontaneous curvature radius and long scaffolds,  $R_0 = 22$  and  $L_s > 40$ , result in large shells, and thus fewer shells per simulation in comparison to other parameter sets, even though the fraction of subunits in shells is similar.

**Connecting Simulation Nondimensional Units to Physical Values.** Although the model is designed to be generic, we are particularly motivated by  $\alpha$ -carboxysomes. We can approximately map our computational model to carboxysomes by setting the cargo diameter (the unit length scale in the model) to that of the rubisco

holoenzyme, implying  $r_* \approx 13$  nm. However, to enable tractable simulation of long assembly time scales, we have set the size ratios of subunit/cargo and scaffold bead/cargo to be larger than the ratios of these proteins relative to rubisco. In particular, our model subunits have a side length of  $r_*$  and are thus about three times larger than carboxysome hexamers (side length  $\approx 4$  nm). To represent the carboxysome system as closely as possible despite this approximation, we have set the bending modulus of the computational model to obtain a characteristic elastic length scale  $R_E = \sqrt{2a\kappa/k_B T}$  similar to that of carboxysomes. Nanoindentation measurements on  $\beta$ -carboxysome shells obtained  $\kappa \approx 25k_B T$ <sup>181</sup> (smaller than that for a typical viral capsid), resulting in an elastic length scale of  $R_E \approx 47$  nm. Correspondingly, we set the computational bending modulus to about  $5-10k_B T$  (see SI Section S2, Computational Model Details), and thus  $R_E \approx 38-54$  nm (using a subunit area  $a \approx 2.5r_*^2$ ).

We perform a similar approximate mapping for the model scaffold molecule, by attempting to match its end-to-end vector (when unconfined) to that of a CsoS2 molecule. The model scaffold behaves as a self-avoiding polymer with a statistical segment length of about one segment, or  $l_k \approx 0.5r_*$ , and thus has an end-to-end vector  $R_{\text{scaf}} \approx l_k N_s^{0.58} r_*$ , with  $N_s = L_s/l_k$  (see SI Figure S2), with a proportional radius of gyration. Since most of the CsoS2 sequence is thought to be intrinsically disordered, we assume that it also behaves as a self-avoiding polymer. The *Halothiobacillus neapolitanus* CsoS2 molecule studied in mutagenesis experiments has 869 amino acids. While its radius of gyration has not been reported, the *Prochlorococcus* CsoS2 with a similar sequence length (792 amino acids) has a radius of gyration of  $\sim 70$  nm.<sup>43</sup> To match this value, we assign the wild-type length of the model scaffold to be  $L_s = 24r_*$  (48 beads).

All visualizations were obtained using VMD.<sup>182</sup>

A preprint of this work is published in ref 183.

## ASSOCIATED CONTENT

### Supporting Information

The Supporting Information is available free of charge at <https://pubs.acs.org/doi/10.1021/acsnano.0c05715>.

Animation of assembly trajectory of one-step assembly pathway leading to full shells, corresponding to Figure 2A (MP4)

Animation of assembly trajectory of one-step assembly with sparse cargo loading, corresponding to Figure 2B (MP4)

Animation of assembly trajectory of two-step assembly pathway corresponding to Figure 2C (MP4)

Supplementary figures, derivations of equilibrium theory predictions, and computational model details (PDF)

## AUTHOR INFORMATION

### Corresponding Author

**Michael F. Hagan** — *Martin A. Fisher School of Physics, Brandeis University, Waltham, Massachusetts 02453, United States*;  [orcid.org/0000-0002-9211-2434](https://orcid.org/0000-0002-9211-2434); Email: [hagan@brandeis.edu](mailto:hagan@brandeis.edu)

### Authors

**Farzaneh Mohajerani** — *Martin A. Fisher School of Physics, Brandeis University, Waltham, Massachusetts 02453, United States*;  [orcid.org/0000-0002-9340-3305](https://orcid.org/0000-0002-9340-3305)

**Evan Sayer** — *Martin A. Fisher School of Physics, Brandeis University, Waltham, Massachusetts 02453, United States*

**Christopher Neil** — *Department of Biochemistry, Brandeis University, Waltham, Massachusetts 02453, United States*

**Koe Inlow** — *Department of Biochemistry, Brandeis University, Waltham, Massachusetts 02453, United States*;  [orcid.org/0000-0002-2535-9613](https://orcid.org/0000-0002-2535-9613)

Complete contact information is available at: <https://pubs.acs.org/10.1021/acsnano.0c05715>

### Notes

The authors declare no competing financial interest.

## ACKNOWLEDGMENTS

We are grateful to Luke Oltrogge and David Savage for insightful discussions. This work was supported by Award Number R01GM108021 from the National Institute of General Medical Sciences and the Brandeis Center for Bioinspired Soft Materials, an NSF MRSEC, DMR-1420382 and DMR-2011846. Computational resources were provided by NSF XSEDE computing resources (XStream, Bridges, and Comet) and the Brandeis HPCC, which is partially supported by DMR-2011486.

## REFERENCES

- Brangwynne, C. P. Phase Transitions and Size Scaling of Membrane-Less Organelles. *J. Cell Biol.* **2013**, *203*, 875–881.
- Weber, S. C.; Brangwynne, C. P. Getting RNA and Protein in Phase. *Cell* **2012**, *149*, 1188–1191.
- Hyman, A. A.; Brangwynne, C. P. Beyond Stereospecificity: Liquids and Mesoscale Organization of Cytoplasm. *Dev. Cell* **2011**, *21*, 14–16.
- Hyman, A. A.; Simons, K. Beyond Oil and Waterphase Transitions in Cells. *Science* **2012**, *337*, 1047–1049.
- Yeates, T. O.; Kerfeld, C. A.; Heinhorst, S.; Cannon, G. C.; Shively, J. M. Protein-Based Organelles in Bacteria: Carboxysomes and Related Microcompartments. *Nat. Rev. Microbiol.* **2008**, *6*, 681–691.
- Nott, T. J.; Petsalaki, E.; Farber, P.; Jervis, D.; Fussner, E.; Plochowietz, A.; Craggs, T. D.; Bazett-Jones, D. P.; Pawson, T.; Forman-Kay, J. D. Phase Transition of a Disordered Nuage Protein Generates Environmentally Responsive Membraneless Organelles. *Mol. Cell* **2015**, *57*, 936–947.
- Zaslavsky, B. Y.; Ferreira, L. A.; Darling, A. L.; Uversky, V. N. The Solvent Side of Proteinaceous Membrane-Less Organelles in Light of Aqueous Two-Phase Systems. *Int. J. Biol. Macromol.* **2018**, *117*, 1224–1251.
- Kerfeld, C. A.; Heinhorst, S.; Cannon, G. C. Bacterial Microcompartments. *Annu. Rev. Microbiol.* **2010**, *64*, 391.
- Tanaka, S.; Kerfeld, C. A.; Sawaya, M. R.; Cai, F.; Heinhorst, S.; Cannon, G. C.; Yeates, T. O. Atomic-Level Models of the Bacterial Carboxysome Shell. *Science* **2008**, *319*, 1083–1086.
- Rae, B. D.; Long, B. M.; Badger, M. R.; Price, G. D. Functions, Compositions, and Evolution of the Two Types of Carboxysomes: Polyhedral Microcompartments That Facilitate CO<sub>2</sub> Fixation in Cyanobacteria and Some Proteobacteria. *Microbiol. Mol. Biol. Rev.* **2013**, *77*, 357–379.
- Bobik, T. A.; Lehman, B. P.; Yeates, T. O. Bacterial Microcompartments: Widespread Prokaryotic Organelles for Isolation and Optimization of Metabolic Pathways. *Mol. Microbiol.* **2015**, *98*, 193–207.
- Chowdhury, C.; Sinha, S.; Chun, S.; Yeates, T. O.; Bobik, T. A. Diverse Bacterial Microcompartment Organelles. *Microbiol. Mol. Biol. Rev.* **2014**, *78*, 438–68.
- Kerfeld, C. A.; Melnicki, M. R. Assembly, Function and Evolution of Cyanobacterial Carboxysomes. *Curr. Opin. Plant Biol.* **2016**, *31*, 66–75.
- Polka, J. K.; Hays, S. G.; Silver, P. A. Building Spatial Synthetic Biology with Compartments, Scaffolds, and Communities. *Cold Spring Harb. Perspect. Biol.* **2016**, *8*.
- Kerfeld, C. A.; Aussignargues, C.; Zarzycki, J.; Cai, F.; Sutter, M. Bacterial Microcompartments. *Nat. Rev. Microbiol.* **2018**, *16*, 277.
- Schmid, M. F.; Paredes, A. M.; Khant, H. A.; Soyer, F.; Aldrich, H. C.; Chiu, W.; Shively, J. M. Structure of *Halothiobacillus*

neapolitanus Carboxysomes by Cryo-Electron Tomography. *J. Mol. Biol.* **2006**, *364*, 526–535.

(17) Iancu, C. V.; Ding, H. J.; Morris, D. M.; Dias, D. P.; Gonzales, A. D.; Martino, A.; Jensen, G. J. The Structure of Isolated Synechococcus Strain WH8102 Carboxysomes as Revealed by Electron Cryotomography. *J. Mol. Biol.* **2007**, *372*, 764–773.

(18) Sutter, M.; Boehringer, D.; Gutmann, S.; Gunther, S.; Prangishvili, D.; Loessner, M. J.; Stetter, K. O.; Weber-Ban, E.; Ban, N. Structural Basis of Enzyme Encapsulation into a Bacterial Nanocompartment. *Nat. Struct. Mol. Biol.* **2008**, *15*, 939–947.

(19) Nichols, R. J.; LaFrance, B.; Phillips, N. R.; Oltrogge, L. M.; Valentin-Alvarado, L. E.; Bischoff, A. J.; Nogales, E.; Savage, D. Discovery and Characterization of a Novel Family of Prokaryotic Nanocompartments Involved in Sulfur Metabolism. *bioRxiv*, 2020; DOI: 10.1101/2020.05.24.113720, accessed June 1, 2020.

(20) Pfeifer, F. Distribution, Formation and Regulation of Gas Vesicles. *Nat. Rev. Microbiol.* **2012**, *10*, 705–715.

(21) Kickhoefer, V. A.; Rajavel, K. S.; Scheffer, G. L.; Dalton, W. S.; Schepers, R. J.; Rome, L. H. Vaults Are Up-Regulated in Multidrug-Resistant Cancer Cell Lines. *J. Biol. Chem.* **1998**, *273*, 8971–8974.

(22) Chesser, A.; Breitling, R.; Takano, E. Bacterial Microcompartments: Biomaterials for Synthetic Biology-Based Compartmentalization Strategies. *ACS Biomater. Sci. Eng.* **2015**, *1*, 345–351.

(23) Lehman, B. P.; Chowdhury, C.; Bobik, T. A. The N Terminus of the PduB Protein Binds the Protein Shell of the Pdu Microcompartment to Its Enzymatic Core. *J. Bacteriol.* **2017**, *199*.

(24) Long, B. M.; Badger, M. R.; Whitney, S. M.; Price, G. D. Analysis of Carboxysomes from Synechococcus PCC7942 Reveals Multiple Rubisco Complexes with Carboxysomal Proteins CcmM and CcaA. *J. Biol. Chem.* **2007**, *282*, 29323–35.

(25) Long, B. M.; Tucker, L.; Badger, M. R.; Price, G. D. Functional Cyanobacterial Beta-Carboxysomes Have an Absolute Requirement for Both Long and Short Forms of the CcmM Protein. *Plant Physiol.* **2010**, *153*, 285–93.

(26) Mayer, M. J.; Juodeikis, R.; Brown, I. R.; Frank, S.; Palmer, D. J.; Deery, E.; Beal, D. M.; Xue, W. F.; Warren, M. J. Effect of Bio-Engineering on Size, Shape, Composition and Rigidity of Bacterial Microcompartments. *Sci. Rep.* **2016**, *6*, 36899.

(27) Quin, M. B.; Perdue, S. A.; Hsu, S. Y.; Schmidt-Dannert, C. Encapsulation of Multiple Cargo Proteins within Recombinant Eut Nanocompartments. *Appl. Microbiol. Biotechnol.* **2016**, *100*, 9187–9200.

(28) Slininger Lee, M.; Tullman-Ercek, D. Practical Considerations for the Encapsulation of Multi-Enzyme Cargos within the Bacterial Microcompartment for Metabolic Engineering. *Current Opinion in Systems Biology* **2017**, *5*, 16–22.

(29) Slininger Lee, M. F.; Jakobson, C. M.; Tullman-Ercek, D. Evidence for Improved Encapsulated Pathway Behavior in a Bacterial Microcompartment through Shell Protein Engineering. *ACS Synth. Biol.* **2017**, *6*, 1880–1891.

(30) Hagen, A.; Sutter, M.; Sloan, N.; Kerfeld, C. A. Programmed Loading and Rapid Purification of Engineered Bacterial Microcompartment Shells. *Nat. Commun.* **2018**, *9*, 1–10.

(31) Kinney, J. N.; Salmeen, A.; Cai, F.; Kerfeld, C. a. Elucidating Essential Role of Conserved Carboxysomal Protein CcmN Reveals Common Feature of Bacterial Microcompartment Assembly. *J. Biol. Chem.* **2012**, *287*, 17729–17736.

(32) Ferlez, B.; Sutter, M.; Kerfeld, C. A. A Designed Bacterial Microcompartment Shell with Tunable Composition and Precision Cargo Loading. *Metab. Eng.* **2019**, *54*, 286–291.

(33) Kalnins, G.; Cesle, E.-E.; Jansons, J.; Liepins, J.; Filimonenko, A.; Tars, K. Encapsulation Mechanisms and Structural Studies of GRM2 Bacterial Microcompartment Particles. *Nat. Commun.* **2020**, *11*, 1–13.

(34) Juodeikis, R.; Lee, M. J.; Mayer, M.; Mantell, J.; Brown, I. R.; Verkade, P.; Woolfson, D. N.; Prentice, M. B.; Frank, S.; Warren, M. J. Effect of Metabolosome Encapsulation Peptides on Enzyme Activity, Coaggregation, Incorporation, and Bacterial Microcompartment Formation. *MicrobiologyOpen* **2020**, *9*, e1010.

(35) Künzle, M.; Mangler, J.; Lach, M.; Beck, T. Peptide-Directed Encapsulation of Inorganic Nanoparticles into Protein Containers. *Nanoscale* **2018**, *10*, 22917–22926.

(36) Rochaix, J.-D. The Pyrenoid: An Overlooked Organelle Comes out of Age. *Cell* **2017**, *171*, 28–29.

(37) Wang, H.; Yan, X.; Aigner, H.; Bracher, A.; Nguyen, N. D.; Hee, W. Y.; Long, B.; Price, G. D.; Hartl, F.; Hayer-Hartl, M. Rubisco Condensate Formation by CcmM in  $\beta$ -Carboxysome Biogenesis. *Nature* **2019**, *566*, 131–135.

(38) He, S.; Chou, H.-T.; Matthies, D.; Wunder, T.; Meyer, M. T.; Atkinson, N.; Martinez-Sanchez, A.; Jeffrey, P. D.; Port, S. A.; Patena, W.; He, G.; Chen, V. K.; Hughson, F. M.; McCormick, A. J.; Mueller-Cajar, O.; Engel, B. D.; Zhiheng, Y.; Jonikas, M. C. The Structural Basis of Rubisco Phase Separation in the Pyrenoid. *Nature Plants* **2020**, *6*, 1480–1490.

(39) Meyer, M. T.; Itakura, A. K.; Patena, W.; Wang, L.; He, S.; Emrich-Mills, T.; Lau, C. S.; Yates, G.; Mackinder, L. C.; Jonikas, M. C. Assembly of the Algal CO<sub>2</sub>-Fixing Organelle, the Pyrenoid, Is Guided by a Rubisco-Binding Motif. *Science Advances* **2020**, *6*, eabd2408.

(40) Cameron, J. C.; Wilson, S. C.; Bernstein, S. L.; Kerfeld, C. A. Biogenesis of a Bacterial Organelle: The Carboxysome Assembly Pathway. *Cell* **2013**, *155*, 1131–40.

(41) Chen, A. H.; Robinson-Mosher, A.; Savage, D. F.; Silver, P. A.; Polka, J. K. The Bacterial Carbon-Fixing Organelle Is Formed by Shell Envelopment of Preassembled Cargo. *PLoS One* **2013**, *8*, e76127.

(42) Wunder, T.; Cheng, S. L. H.; Lai, S.-K.; Li, H.-Y.; Mueller-Cajar, O. The Phase Separation Underlying the Pyrenoid-Based Microalgal Rubisco Supercharger. *Nat. Commun.* **2018**, *9*, 1–10.

(43) Cai, F.; Dou, Z.; Bernstein, S. L.; Leverenz, R.; Williams, E. B.; Heinhorst, S.; Shively, J.; Cannon, G. C.; Kerfeld, C. A. Advances in Understanding Carboxysome Assembly in Prochlorococcus and Synechococcus Implicate CsoS2 as a Critical Component. *Life* **2015**, *5*, 1141.

(44) Chaijiraspong, T.; Nichols, R. J.; Kortright, K. E.; Nixon, C. F.; Teng, P. K.; Oltrogge, L. M.; Savage, D. F. Programmed Ribosomal Frameshifting Mediates Expression of the  $\alpha$ -Carboxysome. *J. Mol. Biol.* **2016**, *428*, 153–164.

(45) Oltrogge, L. M.; Chaijiraspong, T.; Chen, A. W.; Bolin, E. R.; Marqusee, S.; Savage, D. F. Multivalent Interactions between CsoS2 and Rubisco Mediate  $\alpha$ -Carboxysome Formation. *Nat. Struct. Mol. Biol.* **2020**, *27*, 281–287.

(46) Perlmuter, J. D.; Mohajerani, F.; Hagan, M. F. Many-Molecule Encapsulation by an Icosahedral Shell. *eLife* **2016**, *5*, e14078.

(47) Mohajerani, F.; Hagan, M. F. The Role of the Encapsulated Cargo in Microcompartment Assembly. *PLoS Comput. Biol.* **2018**, *14*, e1006351.

(48) Rotskoff, G. M.; Geissler, P. L. Robust Nonequilibrium Pathways to Microcompartment Assembly. *Proc. Natl. Acad. Sci. U. S. A.* **2018**, *115*, 6341–6346.

(49) Menon, B. B.; Heinhorst, S.; Shively, J. M.; Cannon, G. C. The Carboxysome Shell Is Permeable to Protons. *J. Bacteriol.* **2010**, *192*, 5881–5886.

(50) Mahinthichaichan, P.; Morris, D. M.; Wang, Y.; Jensen, G. J.; Tajkhorshid, E. Selective Permeability of Carboxysome Shell Pores to Anionic Molecules. *J. Phys. Chem. B* **2018**, *122*, 9110–9118.

(51) Faulkner, M.; Szabó, I.; Weetman, S. L.; Sicard, F.; Huber, R. G.; Bond, P. J.; Rosta, E.; Liu, L.-N. Molecular Simulations Unravel the Molecular Principles That Mediate Selective Permeability of Carboxysome Shell Protein. *Sci. Rep.* **2020**, *10*, 1–14.

(52) Lassila, J. K.; Bernstein, S. L.; Kinney, J. N.; Axen, S. D.; Kerfeld, C. A. Assembly of Robust Bacterial Microcompartment Shells Using Building Blocks from an Organelle of Unknown Function. *J. Mol. Biol.* **2014**, *426*, 2217–28.

(53) Sutter, M.; Greber, B.; Aussignargues, C.; Kerfeld, C. A. Assembly Principles and Structure of a 6.5-MDa Bacterial Microcompartment Shell. *Science* **2017**, *356*, 1293.

(54) Cai, F.; Bernstein, S. L.; Wilson, S. C.; Kerfeld, C. A. Production and Characterization of Synthetic Carboxysome Shells

with Incorporated Luminal Proteins. *Plant Physiol.* **2016**, *170*, 1868–1877.

(55) Fung, S. Y.; Yang, H.; Bhola, P. T.; Sadatmousavi, P.; Muzar, E.; Liu, M.; Chen, P. Self-Assembling Peptide as a Potential Carrier for Hydrophobic Anticancer Drug Ellipticine: Complexation, Release and *in Vitro* Delivery. *Adv. Funct. Mater.* **2009**, *19*, 74–83.

(56) Vilaça, H.; Castro, T.; Costa, F. M.; Melle-Franco, M.; Hilliou, L.; Hamley, I. W.; Castanheira, E. M.; Martins, J. A.; Ferreira, P. M. Self-Assembled RGD Dehydropeptide Hydrogels for Drug Delivery Applications. *J. Mater. Chem. B* **2017**, *5*, 8607–8617.

(57) Hanafy, N. A. N.; El-Kemary, M.; Loporatti, S. Micelles Structure Development as a Strategy to Improve Smart Cancer Therapy. *Cancers* **2018**, *10*, 238.

(58) Gao, C.; Li, H.; Li, Y.; Kewalramani, S.; Palmer, L. C.; David, V. P.; Stupp, S. I.; Olvera de la Cruz, M.; Bedzyk, M. J. Electrostatic Control of Polymorphism in Charged Amphiphile Assemblies. *J. Phys. Chem. B* **2017**, *121*, 1623–1628.

(59) Hpone Myint, K.; Brown, J. R.; Shim, A. R.; Wyslouzil, B. E.; Hall, L. M. Encapsulation of Nanoparticles during Polymer Micelle Formation: A Dissipative Particle Dynamics Study. *J. Phys. Chem. B* **2016**, *120*, 11582–11594.

(60) Kang, M.; Cui, H.; Loverde, S. M. Coarse-Grained Molecular Dynamics Studies of the Structure and Stability of Peptide-Based Drug Amphiphile Filaments. *Soft Matter* **2017**, *13*, 7721–7730.

(61) Lee, M. T.; Vishnyakov, A.; Neimark, A. V. Calculations of Critical Micelle Concentration by Dissipative Particle Dynamics Simulations: The Role of Chain Rigidity. *J. Phys. Chem. B* **2013**, *117*, 10304–10.

(62) Loverde, S. M.; Klein, M. L.; Discher, D. E. Nanoparticle Shape Improves Delivery: Rational Coarse Grain Molecular Dynamics (rCG-MD) of Taxol in Worm-Like PEG-PCL Micelles. *Adv. Mater.* **2012**, *24*, 3823–30.

(63) Loverde, S. M.; Pantano, D. A.; Christian, D. A.; Mahmud, A.; Klein, M. L.; Discher, D. E. Curvature, Rigidity, and Pattern Formation in Functional Polymer Micelles and Vesicles—from Dynamic Visualization to Molecular Simulation. *Curr. Opin. Solid State Mater. Sci.* **2011**, *15*, 277–284.

(64) Spaeth, J. R.; Kevrekidis, I. G.; Panagiotopoulos, A. Z. Dissipative Particle Dynamics Simulations of Polymer-Protected Nanoparticle Self-Assembly. *J. Chem. Phys.* **2011**, *135*, 184903.

(65) Condezo, G. N.; San Martin, C. Localization of Adenovirus Morphogenesis Players, Together with Visualization of Assembly Intermediates and Failed Products, Favor a Model Where Assembly and Packaging Occur Concurrently at the Periphery of the Replication Center. *PLoS Pathog.* **2017**, *13*, e1006320.

(66) Price, G. D.; Badger, M. R. Evidence for the Role of Carboxysomes in the Cyanobacterial CO<sub>2</sub>-Concentrating Mechanism. *Can. J. Bot.* **1991**, *69*, 963–973.

(67) Shively, J. M.; Ball, F.; Brown, D. H.; Saunders, R. E. Functional Organelles in Prokaryotes: Polyhedral Inclusions (Carboxysomes) of *Thiobacillus neapolitanus*. *Science* **1973**, *182*, 584–586.

(68) Shively, J. M.; Ball, F. L.; Kline, B. W. Electron Microscopy of the Carboxysomes (Polyhedral Bodies) of *Thiobacillus neapolitanus*. *J. Bacteriol.* **1973**, *116*, 1405–1411.

(69) Iancu, C. V.; Morris, D. M.; Dou, Z.; Heinhorst, S.; Cannon, G. C.; Jensen, G. J. Organization, Structure, and Assembly of  $\alpha$ -Carboxysomes Determined by Electron Cryotomography of Intact Cells. *J. Mol. Biol.* **2010**, *396*, 105–117.

(70) Sutter, M.; Laughlin, T. G.; Sloan, N. B.; Serwas, D.; Davies, K. M.; Kerfeld, C. A. Structure of a Synthetic  $\beta$ -Carboxysome Shell. *Plant Physiol.* **2019**, *181*, 1050–1058.

(71) Chen, T.; Glotzer, S. C. Simulation Studies of a Phenomenological Model for Elongated Virus Capsid Formation. *Phys. Rev. E* **2007**, *75*, 051504.

(72) Bruinsma, R. F.; Gelbart, W. M.; Reguera, D.; Rudnick, J.; Zandi, R. Viral Self-Assembly as a Thermodynamic Process. *Phys. Rev. Lett.* **2003**, *90*, 248101.

(73) Zandi, R.; Reguera, D.; Bruinsma, R. F.; Gelbart, W. M.; Rudnick, J. Origin of Icosahedral Symmetry in Viruses. *Proc. Natl. Acad. Sci. U. S. A.* **2004**, *101*, 15556–15560.

(74) Berger, B.; Shor, P. W.; Tuckerkellogg, L.; King, J. Local Rule-Based Theory of Virus Shell Assembly. *Proc. Natl. Acad. Sci. U. S. A.* **1994**, *91*, 7732–7736.

(75) Schwartz, R.; Garcea, R. L.; Berger, B. "Local Rules" Theory Applied to Polyomavirus Polymorphic Capsid Assemblies. *Virology* **2000**, *268*, 461–470.

(76) Rapaport, D. Self-Assembly of Polyhedral Shells: A Molecular Dynamics Study. *Phys. Rev. E* **2004**, *70*, 051905.

(77) Nguyen, H. D.; Reddy, V. S.; Brooks, C. L. Invariant Polymorphism in Virus Capsid Assembly. *J. Am. Chem. Soc.* **2009**, *131*, 2606–14.

(78) Elrad, O. M.; Hagan, M. F. Mechanisms of Size Control and Polymorphism in Viral Capsid Assembly. *Nano Lett.* **2008**, *8*, 3850–3857.

(79) Johnston, I. G.; Louis, A. A.; Doye, J. P. K. Modelling the Self-Assembly of Virus Capsids. *J. Phys.: Condens. Matter* **2010**, *22*, 104101.

(80) Rapaport, D. C. Studies of Reversible Capsid Shell Growth. *J. Phys.: Condens. Matter* **2010**, *22*, 104115.

(81) Nguyen, H.; Brooks, C. Generalized Structural Polymorphism in Self-Assembled Viral Particles. *Nano Lett.* **2008**, *8*, 4574.

(82) Mateu, M. G. Assembly, Stability and Dynamics of Virus Capsids. *Arch. Biochem. Biophys.* **2013**, *531*, 65–79.

(83) Hagan, M. F. Modeling Viral Capsid Assembly. *Adv. Chem. Phys.* **2014**, *155*, 1–68.

(84) Perlmutter, J. D.; Hagan, M. F. Mechanisms of Virus Assembly. *Annu. Rev. Phys. Chem.* **2015**, *66*, 217–239.

(85) Bruinsma, R. F.; Klug, W. S. Physics of Viral Shells. *Annu. Rev. Condens. Matter Phys.* **2015**, *6*, 245–268.

(86) Hagan, M. F.; Zandi, R. Recent Advances in Coarse-Grained Modeling of Virus Assembly. *Curr. Opin. Virol.* **2016**, *18*, 36–43.

(87) Rapaport, D. C. Molecular Dynamics Simulation of Reversibly Self-Assembling Shells in Solution Using Trapezoidal Particles. *Phys. Rev. E* **2012**, *86*, 051917.

(88) Rapaport, D. C.; Johnson, J. E.; Skolnick, J. Supramolecular Self-Assembly: Molecular Dynamics Modeling of Polyhedral Shell Formation. *Comput. Phys. Commun.* **1999**, *122*, 231–235.

(89) Mendoza, C. I.; Reguera, D. Shape Selection and Mis-Assembly in Viral Capsid Formation by Elastic Frustration. *eLife* **2020**, *9*, e52525.

(90) Wagner, J.; Zandi, R. The Robust Assembly of Small Symmetric Nanoshells. *Biophys. J.* **2015**, *109*, 956.

(91) Schwartz, R.; Shor, P. W.; Prevelige, P. E.; Berger, B. Local Rules Simulation of the Kinetics of Virus Capsid Self-Assembly. *Biophys. J.* **1998**, *75*, 2626–2636.

(92) Hagan, M. F.; Chandler, D. Dynamic Pathways for Viral Capsid Assembly. *Biophys. J.* **2006**, *91*, 42–54.

(93) Wilber, A. W.; Doye, J. P. K.; Louis, A. A.; Noya, E. G.; Miller, M. A.; Wong, P. Reversible Self-Assembly of Patchy Particles into Monodisperse Icosahedral Clusters. *J. Chem. Phys.* **2007**, *127*, 085106.

(94) Baschek, J. E.; Klein, H. C. R.; Schwarz, U. S. Stochastic Dynamics of Virus Capsid Formation: Direct *versus* Hierarchical Self-Assembly. *BMC Biophys.* **2012**, *5*, 1–18.

(95) Castelnovo, M.; Verdier, T.; Foret, L. Comparing Open and Closed Molecular Self-Assembly. *EPL (Europhysics Letters)* **2014**, *105*, 28006.

(96) Castelnovo, M.; Muriaux, D.; Faivre-Moskalenko, C. Entropic Control of Particle Sizes during Viral Self-Assembly. *New J. Phys.* **2013**, *15*, 035028.

(97) Boettcher, M. A.; Klein, H. C. R.; Schwarz, U. S. Role of Dynamic Capsomere Supply for Viral Capsid Self-Assembly. *Phys. Biol.* **2015**, *12*, 016014.

(98) Fejer, S. N.; Chakrabarti, D.; Wales, D. J. Emergent Complexity from Simple Anisotropic Building Blocks: Shells, Tubes, and Spirals. *ACS Nano* **2010**, *4*, 219–228.

(99) Kusters, R.; Lin, H.-K.; Zandi, R.; Tsvetkova, I.; Dragnea, B.; van der Schoot, P. Role of Charge Regulation and Size Polydispersity in Nanoparticle Encapsulation by Viral Coat Proteins. *J. Phys. Chem. B* **2015**, *119*, 1869–1880.

(100) Zandi, R.; van der Schoot, P. Size Regulation of ss-RNA Viruses. *Biophys. J.* **2009**, *96*, 9–20.

(101) Hagan, M. F. Controlling Viral Capsid Assembly with Templating. *Phys. Rev. E* **2008**, *77*, 051904.

(102) Hagan, M. F. A Theory for Viral Capsid Assembly around Electrostatic Cores. *J. Chem. Phys.* **2009**, *130*, 114902.

(103) Belyi, V. A.; Muthukumar, M. Electrostatic Origin of the Genome Packing in Viruses. *Proc. Natl. Acad. Sci. U. S. A.* **2006**, *103*, 17174–17178.

(104) Twarock, R.; Bingham, R. J.; Dykeman, E. C.; Stockley, P. G. A Modelling Paradigm for RNA Virus Assembly. *Curr. Opin. Virol.* **2018**, *31*, 74–81.

(105) Zandi, R.; Dragnea, B.; Travasset, A.; Podgornik, R. On Virus Growth and Form. *Phys. Rep.* **2020**, *847*, 1–102.

(106) Li, S.; Roy, P.; Travasset, A.; Zandi, R. Why Large Icosahedral Viruses Need Scaffolding Proteins. *Proc. Natl. Acad. Sci. U. S. A.* **2018**, *115*, 10971–10976.

(107) Li, S.; Zandi, R.; Travasset, A.; Grason, G. M. Ground States of Crystalline Caps: Generalized Jellium on Curved Space. *Phys. Rev. Lett.* **2019**, *123*, 145501.

(108) van der Schoot, P.; Zandi, R. Impact of the Topology of Viral RNAs on Their Encapsulation by Virus Coat Proteins. *J. Biol. Phys.* **2013**, *39*, 289–299.

(109) Erdemci-Tandogan, G.; Wagner, J.; van der Schoot, P.; Podgornik, R.; Zandi, R. RNA Topology Remolds Electrostatic Stabilization of Viruses. *Phys. Rev. E* **2014**, *89*, 032707.

(110) Siber, A.; Zandi, R.; Podgornik, R. Thermodynamics of Nanospheres Encapsulated in Virus Capsids. *Phys. Rev. E* **2010**, *81*, 051919.

(111) Dykeman, E. C.; Stockley, P. G.; Twarock, R. Packaging Signals in Two Single-Stranded RNA Viruses Imply a Conserved Assembly Mechanism and Geometry of the Packaged Genome. *J. Mol. Biol.* **2013**, *425*, 3235–49.

(112) Patel, N.; Dykeman, E. C.; Coutts, R. H. A.; Lomonosoff, G. P.; Rowlands, D. J.; Phillips, S. E. V.; Ranson, N.; Twarock, R.; Tuma, R.; Stockley, P. G. Revealing the Density of Encoded Functions in a Viral RNA. *Proc. Natl. Acad. Sci. U. S. A.* **2015**, *112*, 2227–2232.

(113) Dykeman, E. C.; Stockley, P. G.; Twarock, R. Solving a Levinthal's Paradox for Virus Assembly Identifies a Unique Antiviral Strategy. *Proc. Natl. Acad. Sci. U. S. A.* **2014**, *111*, 5361–5366.

(114) Dykeman, E. C.; Stockley, P. G.; Twarock, R. Building a Viral Capsid in the Presence of Genomic RNA. *Phys. Rev. E* **2013**, *87*, 022717.

(115) Morton, V. L.; Dykeman, E. C.; Stonehouse, N. J.; Ashcroft, A. E.; Twarock, R.; Stockley, P. G. The Impact of Viral RNA on Assembly Pathway Selection. *J. Mol. Biol.* **2010**, *401*, 298–308.

(116) Zhang, R.; Wernersson, E.; Linse, P. Icosahedral Capsid Formation by Capsomer Subunits and a Semiflexible Polyion. *RSC Adv.* **2013**, *3*, 25258–25267.

(117) Zhang, R.; Linse, P. Topological Effects on Capsomer-Polyion Co-Assembly. *J. Chem. Phys.* **2014**, *140*, 244903.

(118) Zhang, R.; Linse, P. Icosahedral Capsid Formation by Capsomers and Short Polyions. *J. Chem. Phys.* **2013**, *138*, 154901.

(119) Angelescu, D. G.; Stenhammar, J.; Linse, P. Packaging of a Flexible Polyelectrolyte inside a Viral Capsid: Effect of Salt Concentration and Salt Valence. *J. Phys. Chem. B* **2007**, *111*, 8477–8485.

(120) Angelescu, D. G.; Linse, P. Monte Carlo Simulations of Flexible Polyelectrolytes inside Viral Capsids with Dodecahedral Charge Distribution. *Phys. Rev. E* **2007**, *75*, 051905.

(121) Panahandeh, S.; Li, S.; Zandi, R. The Equilibrium Structure of Self-Assembled Protein Nano-Cages. *Nanoscale* **2018**, *10*, 22802–22809.

(122) Panahandeh, S.; Li, S.; Marichal, L.; Leite Rubim, R.; Tresset, G.; Zandi, R. How a Virus Circumvents Energy Barriers to Form Symmetric Shells. *ACS Nano* **2020**, *14*, 3170–3180.

(123) Mahalik, J. P.; Brown, K. A.; Cheng, X.; Fuentes-Cabrera, M. Theoretical Study of the Initial Stages of Self-Assembly of a Carboxysome's Facet. *ACS Nano* **2016**, *10*, 5751–8.

(124) Young, E. J.; Burton, R.; Mahalik, J. P.; Sumpter, B. G.; Fuentes-Cabrera, M.; Kerfeld, C. A.; Ducat, D. C. Engineering the Bacterial Microcompartment Domain for Molecular Scaffolding Applications. *Front. Microbiol.* **2017**, *8*, 1441.

(125) Oltrogge, L. M.; Savage, D. F. Unpublished work.

(126) Halperin, A. Polymeric Micelles: A Star Model. *Macromolecules* **1987**, *20*, 2943–2946.

(127) Daoud, M.; Cotton, J. P. Star Shaped Polymers: A Model for the Conformation and Its Concentration Dependence. *J. Phys. (Paris)* **1982**, *43*, 531–538.

(128) Hariharan, R.; Biver, C.; Mays, J.; Russel, W. B. Ionic Strength and Curvature Effects in Flat and Highly Curved Polyelectrolyte Brushes. *Macromolecules* **1998**, *31*, 7506–7513.

(129) Manandhar, A.; Kang, M.; Chakraborty, K.; Tang, P. K.; Loverde, S. M. Molecular Simulations of Peptide Amphiphiles. *Org. Biomol. Chem.* **2017**, *15*, 7993–8005.

(130) Lee, S. M.; Bond, N.; Callaway, C.; Clark, B.; Farmer, E.; Mallard, M.; Jang, S. S. Dissipative Particle Dynamics Simulation of Multicompartment Micelle Nanoreactor with Channel for Reactants. *RSC Adv.* **2018**, *8*, 37866–37871.

(131) Ryan, P.; Forrester, T. J.; Wroblewski, C.; Kenney, T. M.; Kitova, E. N.; Klassen, J. S.; Kimber, M. S. The Small RbcS-Like Domains of the  $\beta$ -Carboxysome Structural Protein CcmM Bind RubisCO at a Site Distinct from that Binding the RbcS Subunit. *J. Biol. Chem.* **2019**, *294*, 2593–2603.

(132) Sutter, M.; Faulkner, M.; Aussignargues, C.; Paasch, B. C.; Barrett, S.; Kerfeld, C. A.; Liu, L.-N. Visualization of Bacterial Microcompartment Facet Assembly Using High-Speed Atomic Force Microscopy. *Nano Lett.* **2016**, *16*, 1590–1595. PMID: 26617073

(133) Kennedy, N. W.; Hershewe, J. M.; Nichols, T. M.; Roth, E. W.; Wilke, C. D.; Mills, C. E.; Jewett, M. C.; Tullman-Ercek, D. Apparent Size and Morphology of Bacterial Microcompartments Varies with Technique. *PLoS One* **2020**, *15*, e0226395.

(134) Huber, I.; Palmer, D. J.; Ludwig, K. N.; Brown, I. R.; Warren, M. J.; Frunzke, J. Construction of Recombinant Pdu Metabolosome Shells for Small Molecule Production in *Corynebacterium glutamicum*. *ACS Synth. Biol.* **2017**, *6*, 2145–2156.

(135) Lee, M. J.; Mantell, J.; Hodgson, L.; Alibhai, D.; Fletcher, J. M.; Brown, I. R.; Frank, S.; Xue, W. F.; Verkade, P.; Woolfson, D. N.; Warren, M. J. Engineered Synthetic Scaffolds for Organizing Proteins within the Bacterial Cytoplasm. *Nat. Chem. Biol.* **2018**, *14*, 142–147.

(136) Pang, A.; Frank, S.; Brown, I.; Warren, M. J.; Pickersgill, R. W. Structural Insights into Higher Order Assembly and Function of the Bacterial Microcompartment Protein PduA. *J. Biol. Chem.* **2014**, *289*, 22377–84.

(137) Uddin, I.; Frank, S.; Warren, M. J.; Pickersgill, R. W. A Generic Self-Assembly Process in Microcompartments and Synthetic Protein Nanotubes. *Small* **2018**, *14*, e1704020.

(138) Hagen, A. R.; Plegaria, J. S.; Sloan, N.; Ferlez, B.; Aussignargues, C.; Burton, R.; Kerfeld, C. A. In Vitro Assembly of Diverse Bacterial Microcompartment Shell Architectures. *Nano Lett.* **2018**, *18*, 7030–7037.

(139) Huang, J.; Ferlez, B. H.; Young, E. J.; Kerfeld, C. A.; Kramer, D. M.; Ducat, D. C. Functionalization of Bacterial Microcompartment Shell Proteins with Covalently Attached Heme. *Front. Bioeng. Biotechnol.* **2020**, *7*, 432.

(140) Young, E. J.; Sakkos, J. K.; Huang, J.; Wright, J. K.; Kachel, B.; Fuentes-Cabrera, M.; Kerfeld, C. A.; Ducat, D. C. Visualizing *in Vivo* Dynamics of Designer Nanoscaffolds. *Nano Lett.* **2020**, *20*, 208–217.

(141) Dryden, K. A.; Crowley, C. S.; Tanaka, S.; Yeates, T. O.; Yeager, M. Two-Dimensional Crystals of Carboxysome Shell Proteins Recapitulate the Hexagonal Packing of Three-Dimensional Crystals. *Protein Sci.* **2009**, *18*, 2629–2635.

(142) Kerfeld, C. A.; Sutter, M. Engineered Bacterial Microcompartments: Apps for Programming Metabolism. *Curr. Opin. Biotechnol.* **2020**, *65*, 225–232.

(143) Zlotnick, A.; Johnson, J. M.; Wingfield, P. W.; Stahl, S. J.; Endres, D. A Theoretical Model Successfully Identifies Features of Hepatitis B Virus Capsid Assembly. *Biochemistry* **1999**, *38*, 14644–14652.

(144) Endres, D.; Zlotnick, A. Model-Based Analysis of Assembly Kinetics for Virus Capsids or Other Spherical Polymers. *Biophys. J.* **2002**, *83*, 1217–1230.

(145) Zlotnick, A. Are Weak Protein-Protein Interactions the General Rule in Capsid Assembly? *Virology* **2003**, *315*, 269–274.

(146) Ceres, P.; Zlotnick, A. Weak Protein-Protein Interactions Are Sufficient to Drive Assembly of Hepatitis B Virus Capsids. *Biochemistry* **2002**, *41*, 11525–11531.

(147) Jack, R. L.; Hagan, M. F.; Chandler, D. Fluctuation-Dissipation Ratios in the Dynamics of Self-Assembly. *Phys. Rev. E* **2007**, *76*, 021119.

(148) Rapaport, D. Role of Reversibility in Viral Capsid Growth: A Paradigm for Self-Assembly. *Phys. Rev. Lett.* **2008**, *101*, 186101.

(149) Whitelam, S.; Feng, E. H.; Hagan, M. F.; Geissler, P. L. The Role of Collective Motion in Examples of Coarsening and Self-Assembly. *Soft Matter* **2009**, *5*, 1251–1262.

(150) Nguyen, H. D.; Reddy, V. S.; Brooks, C. L. Deciphering the Kinetic Mechanism of Spontaneous Self-Assembly of Icosahedral Capsids. *Nano Lett.* **2007**, *7*, 338–344.

(151) Wilber, A. W.; Doye, J. P.; Louis, A. A.; Lewis, A. C. Monodisperse Self-Assembly in a Model with Protein-Like Interactions. *J. Chem. Phys.* **2009**, *131*, 11B602.

(152) Hagan, M. F.; Elrad, O. M.; Jack, R. L. Mechanisms of Kinetic Trapping in Self-Assembly and Phase Transformation. *J. Chem. Phys.* **2011**, *135*, 104115.

(153) Cheng, S.; Fan, C.; Sinha, S.; Bobik, T. A. The PduQ Enzyme Is an Alcohol Dehydrogenase Used to Recycle NAD<sup>+</sup> Internally within the Pdu Microcompartment of *Salmonella Enterica*. *PLoS One* **2012**, *7*, e47144.

(154) Whitelam, S. Hierarchical Assembly May Be a Way to Make Large Information-Rich Structures. *Soft Matter* **2015**, *11*, 8225–8235.

(155) Lázaro, G. R.; Mukhopadhyay, S.; Hagan, M. F. Why Enveloped Viruses Need Cores: The Contribution of a Nucleocapsid Core to Viral Budding. *Biophys. J.* **2018**, *114*, 619–630.

(156) Dai, W.; Chen, M.; Myers, C.; Lutke, S. J.; Pettitt, B. M.; King, J. A.; Schmid, M. F.; Chiu, W. Visualizing Individual RuBisCO and Its Assembly into Carboxysomes in Marine Cyanobacteria by Cryo-Electron Tomography. *J. Mol. Biol.* **2018**, *430*, 4156–4167.

(157) Alexander, S. Adsorption of Chain Molecules with a Polar Head a Scaling Description. *J. Phys. (Paris)* **1977**, *38*, 983–987.

(158) Witten, T. A.; Pincus, P. A. Colloid Stabilization by Long Grafted Polymers. *Macromolecules* **1986**, *19*, 2509–2513.

(159) Zhulina, E. B.; Borisov, O. V. Absorption of a Polyelectrolyte Brush into an Oppositely Charged Layer. *Macromolecules* **1998**, *31*, 7413–7422.

(160) Hagan, M. F.; Grason, G. M. Equilibrium Mechanisms of Self-Limiting Assembly. *arXiv.2007.01927* **2020**, <https://arxiv.org/abs/2007.01927>.

(161) de Gennes, P. *Scaling Concepts in Polymer Physics*; Cornell University Press: Ithaca, 1979.

(162) Heinhorst, S.; Cannon, G. C.; Shively, J. M. *Complex Intracellular Structures in Prokaryotes*; Springer: Berlin, 2006.

(163) Paquay, S.; Kusumaatmaja, H.; Wales, D. J.; Zandi, R.; van der Schoot, P. Energetically Favoured Defects in Dense Packings of Particles on Spherical Surfaces. *Soft Matter* **2016**, *12*, 5708–5717.

(164) Luque, A.; Reguera, D.; Morozov, A.; Rudnick, J.; Bruinsma, R. Physics of Shell Assembly: Line Tension, Hole Implosion, and Closure Catastrophe. *J. Chem. Phys.* **2012**, *136*, 184507.

(165) Fejer, S. N. Minimalistic Coarse-Grained Modeling of Viral Capsid Assembly. *Progress in molecular biology and translational science* **2020**, *170*, 405–434.

(166) Asor, R.; Schlicksup, C. J.; Zhao, Z.; Zlotnick, A.; Raviv, U. Rapidly Forming Early Intermediate Structures Dictate the Pathway of Capsid Assembly. *J. Am. Chem. Soc.* **2020**, *142*, 7868–7882.

(167) Caspar, D. L.; Klug, A. Physical Principles in the Construction of Regular Viruses. *Cold Spring Harbor Symp. Quant. Biol.* **1962**, *27*, 1–24.

(168) Fan, C.; Cheng, S.; Liu, Y.; Escobar, C. M.; Crowley, C. S.; Jefferson, R. E.; Yeates, T. O.; Bobik, T. a. Short N-Terminal Sequences Package Proteins into Bacterial Microcompartments. *Proc. Natl. Acad. Sci. U. S. A.* **2010**, *107*, 7509–7514.

(169) Aussignargues, C.; Paasch, B. C.; Gonzalez-Esquer, R.; Erbilgin, O.; Kerfeld, C. A. Bacterial Microcompartment Assembly: The Key Role of Encapsulation Peptides. *Commun. Integr. Biol.* **2015**, *8*, e1039755.

(170) Cai, F.; Menon, B. B.; Cannon, G. C.; Curry, K. J.; Shively, J. M.; Heinhorst, S. The Pentameric Vertex Proteins Are Necessary for the Icosahedral Carboxysome Shell to Function as a CO<sub>2</sub> Leakage Barrier. *PLoS One* **2009**, *4*, e7521.

(171) Long, B. M.; Hee, W. Y.; Sharwood, R. E.; Rae, B. D.; Kaines, S.; Lim, Y. L.; Nguyen, N. D.; Massey, B.; Bala, S.; von Caemmerer, S.; Badger, M. R.; Price, G. D. Carboxysome Encapsulation of the CO<sub>2</sub>-Fixing Enzyme Rubisco in Tobacco Chloroplasts. *Nat. Commun.* **2018**, *9*, 3570.

(172) Cheng, S.; Sinha, S.; Fan, C.; Liu, Y.; Bobik, T. A. Genetic Analysis of the Protein Shell of the Microcompartments Involved in Coenzyme B12-Dependent 1,2-Propanediol Degradation by *Salmonella*. *J. Bacteriol.* **2011**, *193*, 1385–92.

(173) Parsons, J. B.; Dinesh, S. D.; Deery, E.; Leech, H. K.; Brindley, A. A.; Heldt, D.; Frank, S.; Smales, C. M.; Lunsdorf, H.; Rambach, A.; Gass, M. H.; Bleloch, A.; McClean, K. J.; Munro, A. W.; Rigby, S. E.; Warren, M. J.; Prentice, M. B. Biochemical and Structural Insights into Bacterial Organelle Form and Biogenesis. *J. Biol. Chem.* **2008**, *283*, 14366–75.

(174) Price, G. D.; Howitt, S. M.; Harrison, K.; Badger, M. R. Analysis of a Genomic DNA Region from the Cyanobacterium *Synechococcus* Sp. Strain PCC7942 Involved in Carboxysome Assembly and Function. *J. Bacteriol.* **1993**, *175*, 2871–2879.

(175) Wheatley, N. M.; Gidaniyan, S. D.; Liu, Y.; Cascio, D.; Yeates, T. O. Bacterial Microcompartment Shells of Diverse Functional Types Possess Pentameric Vertex Proteins. *Protein Sci.* **2013**, *22*, 660–5.

(176) Yeates, T. O.; Crowley, C. S.; Tanaka, S. Bacterial Microcompartment Organelles: Protein Shell Structure and Evolution. *Annu. Rev. Biophys.* **2010**, *39*, 185–205.

(177) Tanaka, S.; Sawaya, M. R.; Yeates, T. O. Structure and Mechanisms of a Protein-Based Organelle in *Escherichia coli*. *Science* **2010**, *327*, 81–84.

(178) Anderson, J. A.; Lorenz, C. D.; Travesset, A. General Purpose Molecular Dynamics Simulations Fully Implemented on Graphics Processing Units. *J. Comput. Phys.* **2008**, *227*, 5342–5359.

(179) Nguyen, T. D.; Phillips, C. L.; Anderson, J. A.; Glotzer, S. C. Rigid Body Constraints Realized in Massively-Parallel Molecular Dynamics on Graphics Processing Units. *Comput. Phys. Commun.* **2011**, *182*, 2307–2313.

(180) <https://hoomd-blue.readthedocs.io/en/stable/units.html>, date of access 06.30.2020.

(181) Faulkner, M.; Rodriguez-Ramos, J.; Dykes, G. F.; Owen, S. V.; Casella, S.; Simpson, D. M.; Beynon, R. J.; Liu, L.-N. Direct Characterization of the Native Structure and Mechanics of Cyanobacterial Carboxysomes. *Nanoscale* **2017**, *9*, 10662–10673.

(182) Humphrey, W.; Dalke, A.; Schulter, K. VMD-Visual Molecular Dynamics. *J. Mol. Graphics* **1996**, *14*, 33–38.

(183) Mohajerani, F.; Sayer, E.; Neil, C.; Inlow, K.; Hagan, M. F. Mechanisms of Scaffold-Mediated Microcompartment Assembly and Size-Control. *bioRxiv*, 2020; DOI: [10.1101/2020.10.14.338509](https://doi.org/10.1101/2020.10.14.338509), accessed Nov 1, 2020.